Fault-Tolerant Attitude Stabilization for Satellites Without Rate Sensor

Bing Xiao, Mingyi Huo, Xuebo Yang, and Youmin Zhang, *Senior Member, IEEE*

***Abstract*—A fault-tolerant control approach without rate sensors is presented for the attitude stabilization of a satellite being developed. External disturbances, reaction wheel faults, actuator saturation, and unavailable angular velocity are addressed. A sliding-mode observer is proposed by using attitude feedback only, and the unavailable angular velocity is estimated by this observer in finite time. Using the attitude and the estimated velocity, another sliding-mode observer is proposed to reconstruct actuator faults and disturbances. It is proven that reconstruction with zero observer error is achieved in finite time. With the reconstructed value, a velocity-free controller is then developed to asymptotically stabilize the attitude. Simulation results are also provided to verify the effectiveness of the proposed approach.**

***Index Terms*—Attitude stabilization, fault reconstruction, fault-tolerant control (FTC), sliding-mode observer.**

I. Introduction

ALTHOUGH satellite attitude control has been extensively studied [1], [2], most of the existing schemes may result in unsatisfactory performance and instability when malfunctions occur in actuators. If an attitude system is not designed with the capability to handle faults, then it will lead to the loss of control of the satellite and even the total loss of the satellite. Inspired by this problem, this paper mainly investigates attitude control with reliability and the required performance guaranteed in the face of actuator faults. This involves the concept of fault-tolerant control (FTC) [3], [4]. The existing approaches of FTC can be classified into two categories, i.e., passive and active. The passive FTC of a satellite system is designed to be robust against a class of possible faults [5], [6]. Active FTC relies on a fault detection and identification (FDI) block that detects and identifies faults online [7]–[10] and then actively reacts to a fault by reconfiguring a controller online. The application of the active FTC to satellite attitude control, particularly the FDI design, has attracted considerable interest [11], [12]. However, those FTC methods can be only applied to an attitude system based on the assumption that direct and exact angular velocity measurement is available.

As discussed in [13], redundant sensors or multiple types of sensors are required and cannot be removed or replaced by virtual sensors to achieve the reliable control of aircraft and spacecraft, with high demands to the safety, reliability, and performance of vehicles and missions. However, as investigated in [14] and [15], the desired attitude maneuvers were accomplished by a designed controller without measurements from gyro/rate sensors in the presence of gyro sensor faults. Such an idea has attracted great attention on satellite design without rate sensors, which is due to the limitations in the mass, size, cost, and power constraints of small satellites. Hence, the use of attitude sensors is only practically important for small satellites or microsatellites [16]. For *satellites without actuator faults*, several attitude controllers have been developed to handle this problem [17]. Sliding-mode control is a well-established scheme for handling disturbances and uncertainties [18], [19]. Based on the same concept, a sliding-mode observer is another solution to output feedback control design. In [20], a discrete-time sliding-mode observer was presented to estimate a state and unknown input for a nonlinear system. In [21], a high-gain observer with a sliding-mode term was proposed to estimate the states of a nonlinear system with disturbances. The application of terminal sliding-mode theory for designing an observer to reconstruct system states in finite time was discussed in [22]. The equivalent control-based sliding-mode observer design methodology was used in [23]. There is also a lot of interest in applying observers for satellite attitude control without velocity measurements [24].

Another issue that needs to be addressed in the attitude FTC design is the constraints in control inputs. All types of actuators for satellite attitude systems have upper bounds on their output torque. If an attitude system is not equipped with a novel control algorithm to solve this kind of nonlinearity, then it may lead to control performance deterioration. For a reaction-wheel-driven attitude control system, using magnetic torque robs or thrusters to dump the excess momentum of reaction wheels is the most applied engineering approach. However, this scheme may not be applicable for mass- and power-limited small satellites. To solve this issue, an antiwindup control was presented in [25].

Manuscript received November 15, 2014; revised February 13, 2015 and March 9, 2015; accepted April 4, 2015. Date of publication May 12, 2015; date of current version October 7, 2015. This work was supported in part by the National Natural Science Foundation of China under Grant 61203122.

B. Xiao is with the College of Engineering, Bohai University, Jinzhou 121013, China (e-mail: bxiaobing@gmail.com).

M. Huo is with the Department of Control Science and Engineering, Harbin Institute of Technology, Harbin 150001, China (e-mail: huomingyi.hit@gmail.com).

X. Yang is with the Research Institute of Intelligent Control and Systems, Harbin Institute of Technology, Harbin 150080, China (e-mail: xueboyang@hit.edu.cn).

Y. Zhang is with the Department of Mechanical and Industrial Engineering, Faculty of Engineering and Computer Science, Concordia University, Montreal, QC H3G 1M8, Canada (e-mail: youmin.zhang@concordia.ca).

Color versions of one or more of the figures in this paper are available online at http://ieeexplore.ieee.org.

Digital Object Identifier 10.1109/TIE.2015.2432107

In [26], a nonlinear scheme using a backstepping technique to reduce the peak control torque was derived.

To the best knowledge of the authors, *there are few or even no results on investigating satellite attitude control system design with actuator faults, disturbances, the unmeasured angular velocity, and actuator saturation all addressed simultaneously*. More specifically, as discussed in [3], an integrated design to handle the aforementioned four practical problems is still an open problem. Motivated by solving this challenging problem, this paper presents a unified approach for attitude stabilization control. The issues with regard to the robust control of external disturbances and the reliable control of actuator faults are explicitly addressed. The main contributions of this paper are summarized as follows.

- The proposed scheme is able to tolerate actuator faults. The developed controller has great fault-tolerant capability, and the closed-loop attitude system is asymptotically stabilized.
- The controller designed to stabilize the satellite attitude does not necessitate the angular velocity. It can protect the control from actuator position saturation. The satellite can be thus designed without gyro/rate sensors to measure the velocity and without magnetic torquers to dump the excess momentum of reaction wheels. Reducing the mass and cost of the attitude control system design is met.

This paper is organized as follows. The description of the satellite considered is presented in Section II. The mathematical model of the satellite attitude system, actuator faults, and control problems are given in Section III. A fault-tolerant attitude control approach is proposed in Section IV, and actuator faults, external disturbances, actuator saturation, and the unmeasured angular velocity are all addressed simultaneously. Simulation results are provided in Section V. Conclusions and future work are given in Section VI.

Notations: $\boldsymbol{I}_n \in \Re^{n\times n}$ represents the identity matrix. $\|\cdot\|$ stands for the standard Euclidean norm or its induced norm. $\lambda_{\min}(\boldsymbol{A})$ and $\boldsymbol{A}^{\dagger}$ denote the minimum eigenvalue and the pseudoinverse of a matrix $\boldsymbol{A} \in \Re^{m\times n}$, respectively. For a vector $\boldsymbol{a} = [a_1 \;\; a_2 \;\; a_3]^T \in \Re^3$ and a positive scalar $\ell \in \Re$, the following notations are used in the paper: $\lfloor \boldsymbol{a} \rceil^{\ell} = [|a_1|^{\ell} \;\; \mathrm{sgn}(a_1) \;\; |a_2|^{\ell} \;\; \mathrm{sgn}(a_2) \;\; |a_3|^{\ell} \;\; \mathrm{sgn}(a_3)]^T$, $\mathbf{sgn}(\boldsymbol{a}) = [\mathrm{sgn}(a_1) \;\; \mathrm{sgn}(a_2) \;\; \mathrm{sgn}(a_3)]^T$, and $\mathbf{tanh}(\boldsymbol{a}) = [\tanh(a_1) \;\; \tanh(a_2) \;\; \tanh(a_3)]^T$; here, $\mathrm{sgn}(\cdot)$ and $\tanh(\cdot)$ are the signum and the tangent function, respectively.

II. Description of Satellite

A. Main Parameters and Hardware Resources

A microsatellite being developed in the detailed design phase consists of a cubic structure with a size of 500 mm × 500 mm × 500 mm. Its payload includes a push-broom-type remote sensing camera and an antenna. Taking the high-resolution images of specific high-priority areas is the main mission of the satellite. The antenna is used to communicate with ground stations for receiving commands and downloading data. The orbit of the satellite is circular, with an altitude of 650 km and an inclination of 94.5°. Its orbital rate is $\omega_0 = 0.00109$ rad/s, with an orbital period of $O_T = 5893.69$ s. The satellite mass is about 45 kg. The principal moments of inertia are 20.0, 22.5, and 25.2 kg · m^2, respectively. The products of inertia are smaller than 0.2 kg · m^2 and can be thus neglected.

Since there is a requirement of high pointing accuracy in the high-quality images taken by the satellite, a sophisticated attitude determination and control system for three-axis stabilization is necessary. A pointing accuracy of 0.005° with a stability of 0.0012°/s of the platform has to be achieved for quality images and stored image data transmission. Due to its small size and with cost consideration, it is desirable without gyro/rate sensors installed on the satellite. Hence, the stabilizing attitude by only using attitude sensors is investigated for this satellite in this paper. Consequently, only one three-axis magnetometer, two solid-state horizon sensors, and one two-axis coarse sun sensor are equipped to measure the satellite's attitude. There is no rate gyro mounted to measure the angular velocity of the satellite. To increase the attitude control reliability, the satellite uses four reaction wheels for *attitude stabilization*. Three wheels are mounted orthogonally, which are aligned with the satellite body axes, i.e., $+X$, $+Y$, and $+Z$, respectively, and a fourth redundant wheel is mounted skewed at equal angles (54.7°) to each of the body axes, which is diagonally aligned in the $+X$, $+Y$, $+Z$ quadrant. To solve the potential saturation problem of reaction wheels, three magnetic torque rods are additionally equipped to unload the saturated control power. The maximum torque $u_{\max}$ generated by each reaction wheel is 0.1 N · m, i.e., $u_{\max} = 0.1$ N · m.

Six orbit control thrusters (orbit control system (OCS) thrusters) are symmetrically distributed on the three axes of the body-fixed frame for orbital maneuvers. The propulsion force is perpendicular to the corresponding axis. To perform the mission of image taking, a large-angle attitude maneuver is usually required and should be accomplished in a short time. The OCS thrusters are thus used for the attitude control to take images because thrusters can supply larger torque than reaction wheels.

B. Attitude Maneuver Sequence in Planned Missions

Fig. 1 illustrates the fundamental operation modes of the satellite. Among these modes, taking images in a sunlight condition and downloading image data during an eclipse period are two main and challenging missions. An attitude stabilization maneuver is started at point $\mathbf{A}$, where the sunlight is tangent to the orbit. This maneuver ensures the satellite to be oriented toward the Earth during the eclipse period. Data such as images can be thus downloaded to a ground station. When the satellite is at point $\mathbf{B}$, a large-angle attitude maneuver is going to be performed. The mounted charge-coupled-device camera is ensured to be toward specific high-priority areas, and high-resolution images are taken.

In any imaging or communication mission, the satellite undergoes a number of attitude maneuvers during each pass above the horizon. The time sequence of the attitude maneuvers used to accomplish the planned two missions is illustrated in Fig. 2. After the satellite separates from the launch vehicle

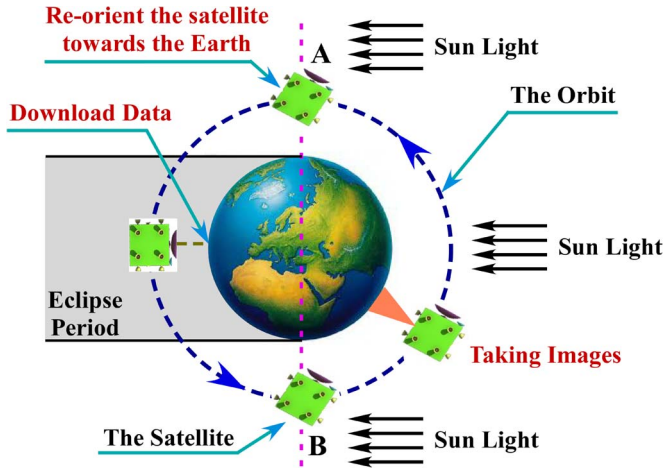

Fig. 1. Operation modes of the satellite.

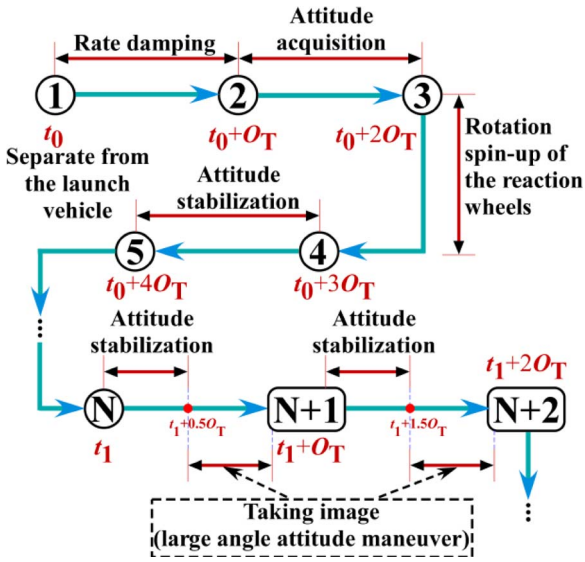

Fig. 2. Time sequence of the attitude maneuvers for the scientific mission.

at $t = t_0$, a rate-damping control maneuver is performed in the first orbital period O_T. Thereafter, an attitude acquisition maneuver is finished during the second orbital period. It then follows the rotation spin-up of the reaction wheels in the third orbital period. Starting in the fourth orbital period, an attitude stabilization maneuver is conducted to establish high pointing accuracy and stability. Suppose that those two planned missions are started at $t = t_1 (t_1 > t_0 + 4O_T)$; the large-angle attitude maneuver and attitude stabilization are alternately conducted in one orbital period.

After the rate-damping and attitude acquisition maneuvers, the angular velocity and the attitude of the satellite are maintained within 1°/s and 0.5°, respectively. Moreover, every time, at the end of the large-angle attitude maneuver for the image-taking mission, the angular velocity and the attitude are planned to be within 2°/s and 1° by using thrusters, respectively. That is, the accomplishment of the image-taking mission will supply the attitude stabilization maneuver for downloading data with a small initial velocity and a small initial attitude angle.

III. Mathematical Model and Problem Formulation

Only the problem of attitude stabilization using reaction wheels is solved in this paper. Therefore, the mathematical model for attitude stabilization is given first.

A. Satellite Model Description

Three coordinate systems are usually used in the attitude control, i.e., the inertial fixed reference coordinate $\mathcal{F}_i$, the orbital coordinate reference $\mathcal{F}_o$, and the body-fixed reference frame $\mathcal{F}_b$. The orientation of the satellite with respect to $\mathcal{F}_o$ is obtained by a yaw–pitch–roll sequence of rotations. For the considered rigid satellite, its model can be given by [27]

$$\boldsymbol{\omega}_{bi} = \boldsymbol{\omega}_{bo} - \boldsymbol{\omega}_c(\boldsymbol{\Theta}) \tag{1}$$

$$\boldsymbol{J}\dot{\boldsymbol{\omega}}_{bi} = -\boldsymbol{\omega}_{bi}^{\times}\boldsymbol{J}\boldsymbol{\omega}_{bi} + \boldsymbol{\tau} + \boldsymbol{d} \tag{2}$$

where $\boldsymbol{\Theta} = [\theta\ \phi\ \psi]^T$ is the attitude Euler angles vector, $\boldsymbol{J} = \mathrm{diag}(J_1, J_2, J_3)$ is the inertia matrix, $\boldsymbol{\tau} \in \Re^3$ is the total torque generated by all reaction wheels, $\boldsymbol{d} \in \Re^3$ is the external disturbance, $\boldsymbol{\omega}_{bi} \in \Re^3$ is the angular velocity of the satellite given in $\mathcal{F}_b$, $\boldsymbol{\omega}_{bo} = \boldsymbol{R}(\boldsymbol{\Theta})\dot{\boldsymbol{\Theta}}$ is the angular velocity in $\mathcal{F}_o$

$$\boldsymbol{R}(\boldsymbol{\Theta}) = \begin{bmatrix} 1 & 0 & -\sin\phi \\ 0 & \cos\theta & \sin\theta\cos\phi \\ 0 & -\sin\theta & \cos\theta\cos\phi \end{bmatrix} \tag{3}$$

$$\boldsymbol{\omega}_c(\boldsymbol{\Theta}) = \omega_0 \begin{bmatrix} \cos\phi\sin\psi \\ \cos\theta\cos\psi + \sin\theta\sin\phi\sin\psi \\ -\sin\theta\cos\psi + \cos\theta\sin\phi\sin\psi \end{bmatrix} \tag{4}$$

and $\times$ is an operator on vector $\boldsymbol{a} \in \Re^3$ such that $\boldsymbol{a}^{\times} = \begin{bmatrix} 0 & -a_3 & a_2 \\ a_3 & 0 & -a_1 \\ -a_2 & a_1 & 0 \end{bmatrix}^T$.

Using (3) and (4), the attitude kinematics can be rewritten as

$$\boldsymbol{\omega}_{bi} = \boldsymbol{\chi} + \Delta\boldsymbol{g}_1(\omega_0, \boldsymbol{\Theta}, \dot{\boldsymbol{\Theta}}) \tag{5}$$

with $\boldsymbol{\chi} = [\dot{\theta} - \omega_0\psi\ \dot{\phi} - \omega_0\ \dot{\psi} + \omega_0\theta]^T$, and $\Delta\boldsymbol{g}_1 = \boldsymbol{R}(\boldsymbol{\Theta})\dot{\boldsymbol{\Theta}} - \boldsymbol{\omega}_c - \boldsymbol{\chi}$. Substituting (5) into (2) gives an important model for the microsatellite attitude dynamics as follows:

$$\boldsymbol{J}\ddot{\boldsymbol{\Theta}} + \boldsymbol{C}\dot{\boldsymbol{\Theta}} + \boldsymbol{K}\boldsymbol{\Theta} + \Delta\boldsymbol{g}_2 + \Delta\boldsymbol{g}_3 = \boldsymbol{\tau} + \boldsymbol{d} \tag{6}$$

where $\Delta\boldsymbol{g}_2 = \Delta\boldsymbol{g}_1^{\times}\boldsymbol{J}(\boldsymbol{\chi} + \Delta\boldsymbol{g}_1) + \boldsymbol{J}(d(\Delta\boldsymbol{g}_1)/dt)$, $\boldsymbol{K} = \omega_0^2\mathrm{diag}(J_2 - J_3, 0, J_2 - J_1)$, $\boldsymbol{C} = \boldsymbol{\omega}_0(J_1 - J_2 + J_3)\begin{bmatrix} 0 & 0 & -1 \\ 0 & 0 & 0 \\ 1 & 0 & 0 \end{bmatrix}$, and

$$\Delta\boldsymbol{g}_3 = \begin{bmatrix} -(J_2 - J_3)\dot{\phi}(\dot{\psi} + \omega_0\theta) \\ (J_1 - J_3)(\dot{\theta}\dot{\psi} + \omega_0\theta\dot{\theta} - \omega_0\psi\dot{\psi} - \omega_0^2\theta\psi) \\ -(J_1 - J_2)\dot{\phi}(\dot{\theta} - \omega_0\dot{\psi}). \end{bmatrix}.$$

As stated in Section II-B, a small attitude deviation in the Euler angles and the angular velocity is guaranteed after attitude acquisition or the image-taking mission. Term $\Delta\boldsymbol{g}_1$ is thus a vector with small values. The angular acceleration of the satellite is also bounded. Hence, $\Delta\boldsymbol{g}_2$ and $\Delta\boldsymbol{g}_3$ are bounded.

In addition to the Euler angles representation, a unit quaternion can be also used to represent the attitude. The corresponding quaternion of Euler angles $\boldsymbol{\Theta}$ is denoted by $\boldsymbol{Q}_e = [e_0 \ \boldsymbol{e}^T]^T \in \Re^4$, where $e_0^2 + \boldsymbol{e}^T\boldsymbol{e} = 1$, and

$$\boldsymbol{Q}_e = \begin{bmatrix} \cos\bar{\theta}\cos\bar{\phi}\cos\bar{\psi} + \sin\bar{\theta}\sin\bar{\phi}\sin\bar{\psi} \\ \sin\bar{\theta}\cos\bar{\phi}\cos\bar{\psi} - \cos\bar{\theta}\sin\bar{\phi}\sin\bar{\psi} \\ \cos\bar{\theta}\sin\bar{\phi}\cos\bar{\psi} + \sin\bar{\theta}\cos\bar{\phi}\sin\bar{\psi} \\ -\sin\bar{\theta}\sin\bar{\phi}\cos\bar{\psi} + \cos\bar{\theta}\cos\bar{\phi}\sin\bar{\psi} \end{bmatrix} = \boldsymbol{f}(\boldsymbol{\Theta}) \quad (7)$$

where $\bar{\theta} = 0.5\theta$, $\bar{\phi} = 0.5\phi$, and $\bar{\psi} = 0.5\psi$.

Using unit quaternion $\boldsymbol{Q}_e$ to represent the satellite attitude, another nonlinear model of the satellite attitude system can be described by [1]

$$\dot{e}_0 = -0.5\boldsymbol{e}^T\boldsymbol{\omega}_{bo} \quad (8)$$

$$\dot{\boldsymbol{e}} = 0.5\left(\boldsymbol{e}^\times + e_0\boldsymbol{I}_3\right)\boldsymbol{\omega}_{bo} \quad (9)$$

$$\boldsymbol{J}\dot{\boldsymbol{\omega}}_{bo} = -\boldsymbol{\omega}_{bo}^\times\boldsymbol{J}\boldsymbol{\omega}_{bo} + \boldsymbol{H}_1 + \boldsymbol{\tau} + \boldsymbol{d} \quad (10)$$

where $\boldsymbol{H}_1 = (\boldsymbol{J}\boldsymbol{\omega}_{bo}^\times - \boldsymbol{\omega}_{bo}^\times\boldsymbol{J})\boldsymbol{R}(\boldsymbol{Q}_e)\boldsymbol{\omega}_{oi} - (\boldsymbol{R}(\boldsymbol{Q}_e)\boldsymbol{\omega}_{oi})^\times\boldsymbol{J}(\boldsymbol{\omega}_e + \boldsymbol{R}(\boldsymbol{Q}_e)\boldsymbol{\omega}_{oi})$, $\boldsymbol{\omega}_{oi} = [0 \quad -\omega_0 \quad 0]^T$, and $\boldsymbol{R}(\boldsymbol{Q}_e) = (e_0^2 - \boldsymbol{e}^T\boldsymbol{e})\boldsymbol{I}_3 + 2\boldsymbol{e}\boldsymbol{e}^T - 2e_0\boldsymbol{e}^\times$. Term $[e_0 \ \boldsymbol{e}^T]$ in (8) and (9) denote the satellite's relative attitude between $\mathcal{F}_b$ and $\mathcal{F}_o$.

For the considered satellite, the aerodynamic torque, the gravity-gradient torque, the solar radiation torque, and the Earth magnetic torque are the primary disturbances for $\boldsymbol{d}$ in (2). Using the calculation in [27] and the satellite's main physical parameters including the altitude and the structure, the upper bound of $\boldsymbol{d}$ can be estimated as $d_{\max} = 2.6 \times 10^{-4}$ N · m, i.e., $\|\boldsymbol{d}(t)\| \le d_{\max}$.

B. Actuator Fault

The attitude stabilization maneuver is planned to be performed using four reaction wheels. Thus, taking reaction wheel faults into account, the total control torque $\boldsymbol{\tau}$ has the following form:

$$\boldsymbol{\tau} = \boldsymbol{D}\boldsymbol{u}, \quad \boldsymbol{u} = \boldsymbol{u}_n + \boldsymbol{B}\left(t - \boldsymbol{T}_f^o\right)\boldsymbol{u}_f \quad (11)$$

where $\boldsymbol{D} = \begin{bmatrix} 1 & 0 & 0 & 1/\sqrt{3} \\ 0 & 1 & 0 & 1/\sqrt{3} \\ 0 & 0 & 1 & 1/\sqrt{3} \end{bmatrix}$ is the reaction wheel distribution matrix, $\boldsymbol{u} \in \Re^4$ is the actual torque generated by four wheels, $\boldsymbol{u}_n \in \Re^4$ denotes the nominal/commanded torque, and term $\boldsymbol{B}(t - \boldsymbol{T}_f^o)\boldsymbol{u}_f \in \Re^4$ denotes the deviation in the output torque due to the occurrence of a fault. Matrix $\boldsymbol{B}(t - \boldsymbol{T}_f^o) \in \Re^4$ denotes the time profiles of a fault that occurs at some *unknown* time $\boldsymbol{T}_f^o = [T_{f1}^o \ T_{f2}^o \ T_{f3}^o \ T_{f4}^o]^T \in \Re^4$, and $\boldsymbol{u}_f$ is the nonlinear fault function. Let fault time profile $\boldsymbol{B}(t - \boldsymbol{T}_f^o)$ be a diagonal matrix of the following form:

$$\boldsymbol{B}\left(t - \boldsymbol{T}_f^o\right) = \mathrm{diag}\left(b_1\left(t - T_{f1}^o\right), b_2\left(t - T_{f2}^o\right), b_3\left(t - T_{f3}^o\right), b_4\left(t - T_{f4}^o\right)\right) \quad (12)$$

where $b_i : \Re \mapsto \Re$ is a function representing the time profile of a fault affecting the ith reaction wheel, $i = 1, 2, 3, 4$, and this profile is modeled by

$$b_i\left(t - T_{fi}^o\right) = \begin{cases} 0, & \text{if } t < T_{fi}^o \\ 1 - e^{-a_i\left(t - T_{fi}^o\right)}, & \text{if } t \ge T_{fi}^o \end{cases} \quad (13)$$

where scalar $a_i > 0$ denotes the unknown fault evolution rate. Small values of a_i characterize slowly developing faults, which are also known as *incipient* faults. For large values of a_i, the time profile of b_i approaches a step function that models an *abrupt* fault.

C. Problem Statement

To provide theoretical support for next-generation microsatellite attitude control subsystem design without rate sensors, the objective of this paper is to design a commanded control $\boldsymbol{u}_n$ to asymptotically stabilize the attitude, i.e., $\boldsymbol{e} \to \boldsymbol{0}$, $e_0 \to 1$, $\boldsymbol{\Theta} \to \boldsymbol{0}$, and $\boldsymbol{\omega}_{bo} \to \boldsymbol{0}$, even in the presence of external disturbances, fault (11), and reaction wheel saturation $u_{\max}$. The controller should be designed with the angular velocity eliminated, i.e., $\boldsymbol{\omega}_e$ and $\dot{\boldsymbol{\Theta}}$ are not required.

IV. Fault-Tolerant Attitude Control Without Angular Velocity Measurements

Define a matrix as $\boldsymbol{P} = 0.5(\boldsymbol{e}^\times + e_0\boldsymbol{I}_3)$; it is obtained from (9) that $\boldsymbol{\omega}_{bo} = \boldsymbol{P}^{-1}(\boldsymbol{Q}_e)\dot{\boldsymbol{e}}$. Substituting this equation into (10) and premultiplying both sides of the resulting expression by $(\boldsymbol{P}^{-1})^T\boldsymbol{J}\boldsymbol{P}^{-1}$, it leads nonlinear attitude model (8)–(10) with faulty input (11) to

$$\boldsymbol{J}^*\ddot{\boldsymbol{e}} + \boldsymbol{C}\dot{\boldsymbol{e}} + \boldsymbol{F}^T\boldsymbol{H}_2 = \boldsymbol{F}^T\left[\boldsymbol{D}\boldsymbol{u}_n + \boldsymbol{D}\boldsymbol{B}(t - T_0)\boldsymbol{u}_f + \boldsymbol{d}\right] \quad (14)$$

where $\boldsymbol{F} = \boldsymbol{P}^{-1}$, $\boldsymbol{C} = \boldsymbol{F}^T\boldsymbol{J}\dot{\boldsymbol{F}} - \boldsymbol{F}^T(\boldsymbol{J}\boldsymbol{F}\dot{\boldsymbol{e}})^\times\boldsymbol{F}$, $\boldsymbol{J}^* = \boldsymbol{F}^T\boldsymbol{J}\boldsymbol{F}$, and $\boldsymbol{H}_2 = [\boldsymbol{J}(\boldsymbol{P}\dot{\boldsymbol{e}})^\times - (\boldsymbol{P}\dot{\boldsymbol{e}})^\times\boldsymbol{J}]\boldsymbol{R}(\boldsymbol{Q}_e)\boldsymbol{\omega}_{oi} - (\boldsymbol{R}(\boldsymbol{Q}_e)\boldsymbol{\omega}_{oi})^\times\boldsymbol{J}(\boldsymbol{P}\dot{\boldsymbol{e}} + \boldsymbol{R}(\boldsymbol{Q}_e)\boldsymbol{\omega}_{oi})$. Note that $\boldsymbol{J}^*$ is symmetric positive definite, and $\dot{\boldsymbol{J}}^* - 2\boldsymbol{C}$ is skew symmetric such that $\boldsymbol{a}^T(\dot{\boldsymbol{J}}^* - 2\boldsymbol{C})\boldsymbol{a} = 0$ for all $\boldsymbol{a} \in \Re^3$.

Remark 1: Obtaining (14) requires that $\boldsymbol{P}$ is invertible. $\det(\boldsymbol{P}) = 0.5e_0(t) \ne 0$ should be guaranteed to avoid the singularity of $\boldsymbol{P}$ for $t \ge 0$. It thus requires the initial conditions such that $e_0(0) \ne 0$ and the subsequently designed controller ensuring that $e_0(t) \ne 0$ for $t > 0$. Regarding the restriction on the initial conditions, it is known from $e_0^2 + \boldsymbol{e}^T\boldsymbol{e} = 1$ that the desired trajectory can be always initialized to meet $e_0(0) \ne 0$. Therefore, the initial condition restriction is actually a very mild restriction on the desired trajectory.

To handle faults and disturbances, $\boldsymbol{D}\boldsymbol{B}(t - \boldsymbol{T}_f^o)\boldsymbol{u}_f$ and $\boldsymbol{d}$ are lumped into a single fault vector $\boldsymbol{u}_l$, i.e., $\boldsymbol{u}_l = \boldsymbol{D}\boldsymbol{B}(t - \boldsymbol{T}_f^o)\boldsymbol{u}_f + \boldsymbol{d}$. In this section, a fault-tolerant attitude control without the angular velocity measurement will be proposed to stabilize the attitude of the satellite. The structure of the closed-loop system is shown in Fig. 3. This control structure includes three modules, i.e., ***a sliding-mode observer*** designed to estimate $\dot{\boldsymbol{\Theta}}$ with zero observer error in finite time, ***a reconstruction module*** synthesized to reconstruct the lumped fault in

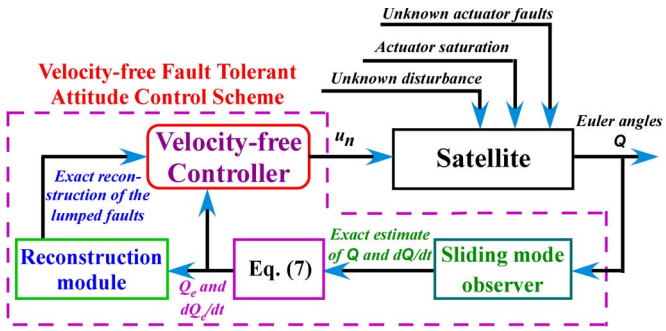

Fig. 3. Proposed fault-tolerant attitude control system of the microsatellite without rate sensors.

finite time, and ***a velocity-free controller*** proposed by using the reconstructed fault information and the satellite attitude. The detailed time sequence of implementing the proposed control scheme is described as follows.

Starting at $t = t_0 + 2O_T$: The measurable attitude Euler angles $\boldsymbol{\Theta}$ are fed back to the sliding-mode observer module to obtain the estimate of $\dot{\boldsymbol{\Theta}}$. At the same time, $\boldsymbol{Q}_e$ and $\dot{\boldsymbol{Q}}_e$ are calculated by using $\boldsymbol{\Theta}$, the estimation of $\dot{\boldsymbol{\Theta}}$, and (7).

Starting at $t = t_0 + 3O_T$: Injecting $\boldsymbol{Q}_e$ and $\dot{\boldsymbol{Q}}_e$ into the reconstruction module, the precise information of lumped fault $\boldsymbol{u}_l$ is obtained.

Suppose that the Stabilization Maneuver is Required to Start at $t_s (t_s \geq t_0 + 3O_T)$: Using attitude $\boldsymbol{Q}_e$ and the reconstructed fault, the controller module should be implemented.

Assumption 1: After the attitude acquisition maneuver and the rotation spin-up of reaction wheel, the satellite attitude satisfies constraint $\|\boldsymbol{F}^T(t_0 + 3O_T)\| d_{\max} \ll u_{\max}$.

Assumption 2: When the rotation spin-up of reaction wheels is finished at $t = t_0 + 3O_T$, all reaction wheels are healthy, i.e., $\boldsymbol{u}_f(t_0 + 3O_T) = \boldsymbol{0}$.

A. Sliding-Mode Observer Design for Θ and $\dot{\Theta}$

Define two new states $\boldsymbol{x}_1 = \boldsymbol{\Theta}$ and $\boldsymbol{x}_2 = \dot{\boldsymbol{\Theta}}$; system (6) with reaction wheel fault (11) can be rewritten as

$$\begin{bmatrix}\dot{\boldsymbol{x}}_1 \\ \dot{\boldsymbol{x}}_2\end{bmatrix} = \begin{bmatrix}\boldsymbol{0} & \boldsymbol{I}_3 \\ -\boldsymbol{J}^{-1}\boldsymbol{K} & -\boldsymbol{J}^{-1}\boldsymbol{C}\end{bmatrix}\begin{bmatrix}\boldsymbol{x}_1 \\ \boldsymbol{x}_2\end{bmatrix} + \begin{bmatrix}\boldsymbol{0} \\ \boldsymbol{J}^{-1}\boldsymbol{D}\left(\boldsymbol{u}_n + \boldsymbol{B}\left(t - \boldsymbol{T}_f^o\right)\boldsymbol{u}_f\right)\end{bmatrix} + \begin{bmatrix}\boldsymbol{0} \\ \boldsymbol{J}^{-1}(\boldsymbol{d} - \Delta\boldsymbol{g}_2 - \Delta\boldsymbol{g}_3)\end{bmatrix}. \tag{15}$$

Because attitude sensors are equipped to measure the satellite attitude, attitude Euler angles $\boldsymbol{\Theta}$ are available. The system output defined by $\boldsymbol{y}_o = \boldsymbol{\Theta}$ is thus available. To estimate states $\boldsymbol{x}_1$ and $\boldsymbol{x}_2$ in finite time, an equivalent output injection sliding-mode observer is proposed as follows:

$$\dot{\hat{\boldsymbol{x}}}_1 = \hat{\boldsymbol{x}}_2 + \lambda_{o1}\mathbf{sgn}(\boldsymbol{y}_o - \hat{\boldsymbol{x}}_1) \tag{16}$$

$$\dot{\hat{\boldsymbol{x}}}_2 = -\boldsymbol{J}^{-1}\boldsymbol{K}\hat{\boldsymbol{x}}_1 - \boldsymbol{J}^{-1}\boldsymbol{C}\hat{\boldsymbol{x}}_2 + \delta_o(\lambda_{o2}\mathbf{sgn}(\tilde{\boldsymbol{x}}_2 - \hat{\boldsymbol{x}}_2)) + \boldsymbol{J}^{-1}\boldsymbol{D}\boldsymbol{u}_n \tag{17}$$

where $\tilde{\boldsymbol{x}}_2 = \hat{\boldsymbol{x}}_2 + (\lambda_{o1}\mathbf{sgn}(\boldsymbol{y}_o - \hat{\boldsymbol{x}}_1))_{\text{eq}}$, and $\hat{\boldsymbol{x}}_i$, $i = 1, 2$, is the estimate of $\boldsymbol{x}_i$. λ_{o1} and λ_{o2} are positive scalars. Term $\delta_o = 0$ if $\boldsymbol{x}_2 - \hat{\boldsymbol{x}}_2 = \boldsymbol{0}$; otherwise, $\delta_o = 1$.

Theorem 1: For plant (6) subject to reaction wheel faults (11) and with observer (16) and (17) applied, there exist λ_{o1} and λ_{o2} such that the estimated states $\hat{\boldsymbol{x}}_i$, $i = 1, 2$, converge to its actual states $\boldsymbol{x}_i$ with zero error in finite time, respectively.

Proof: See the Appendix.

From Theorem 1 and its proof, it is obtained that $\hat{\boldsymbol{x}}_2$ converges to $\boldsymbol{x}_2$ in finite time T_{o2} by only using the measurable attitude $\boldsymbol{\Theta}$, i.e., $\hat{\boldsymbol{x}}_2(t) \equiv \boldsymbol{x}_2(t)$ for all $t \geq T_{o2}$. According to (7), $\boldsymbol{Q}_e$ is differential. Furthermore, $\dot{\boldsymbol{Q}}_e$ can be calculated by differentiating both sides of (7). Denote $\dot{\boldsymbol{Q}}_e$ as $\dot{\boldsymbol{Q}}_e = \dot{\boldsymbol{f}}(\boldsymbol{\Theta}) = \boldsymbol{f}_1(\boldsymbol{\Theta}, \dot{\boldsymbol{\Theta}})$. Therefore, by time T_{o2}, one has

$$\dot{\boldsymbol{Q}}_e = \left[\dot{e}_0\ \dot{\boldsymbol{e}}^T\right]^T = \boldsymbol{f}_1(\boldsymbol{\Theta}, \hat{\boldsymbol{x}}_2). \tag{18}$$

B. Fault Reconstruction Module Design

By introducing generalized inertia $\boldsymbol{J}_g = \boldsymbol{J}^*\dot{\boldsymbol{e}}$, applying skew-symmetric matrix $\dot{\boldsymbol{J}}^* - 2\boldsymbol{C}$ and (14) results in $\dot{\boldsymbol{J}}_g = \boldsymbol{F}^T\boldsymbol{D}\boldsymbol{u}_n - \overline{\boldsymbol{\tau}}_l - \boldsymbol{H}_3$, with $\boldsymbol{H}_3 = -(1/2)\dot{\boldsymbol{e}}^T(\partial\boldsymbol{J}^*/\partial\boldsymbol{e})\dot{\boldsymbol{e}} + \boldsymbol{F}^T\boldsymbol{H}_2$ and $\overline{\boldsymbol{\tau}}_l = -\boldsymbol{F}^T\boldsymbol{u}_l$. Now, a residual vector is defined by

$$\boldsymbol{r}(t) = k_r \int_{t_0 + 3O_T}^{t} \left[\boldsymbol{F}^T\boldsymbol{D}\boldsymbol{u}_n - \boldsymbol{H}_3 - \boldsymbol{r}(s)\right] ds - k_r\boldsymbol{J}_g \tag{19}$$

with $k_r > 0$ as a scalar. This residual satisfies the following dynamics:

$$\dot{\boldsymbol{r}} = -k_r\boldsymbol{r} + k_r\overline{\boldsymbol{\tau}}_l. \tag{20}$$

Based on (7) and (18), it can be seen that $\boldsymbol{r}$ can be obtained with only attitude measurements $\boldsymbol{\Theta}$. Furthermore, because continuous function $\boldsymbol{B}(t - \boldsymbol{T}_f^o)$ in (12) is differentiable, $\overline{\boldsymbol{\tau}}_l$ can be assumed to be a differentiable function with time derivative $\boldsymbol{u}_r \in \Re^3$. The problem of reconstructing the evolution of $\overline{\boldsymbol{\tau}}_l$ can be formulated as observing the state of a linear system driven by residual $\boldsymbol{r}$ and an unknown input. The linear system is expressed as

$$\dot{\boldsymbol{\xi}}_1 = -k_r\boldsymbol{\xi}_1 + k_r\boldsymbol{\xi}_2 \tag{21}$$

$$\dot{\boldsymbol{\xi}}_2 = \boldsymbol{u}_r \tag{22}$$

$$\boldsymbol{y}_r = \boldsymbol{\xi}_1 \tag{23}$$

where $\boldsymbol{\xi}_1 = \boldsymbol{r}$, $\boldsymbol{\xi}_2 = \overline{\boldsymbol{\tau}}_l$, $\boldsymbol{u}_r$ is the unknown input, and $\boldsymbol{y}_r$ is the measurable output.

According to the operating principle of a reaction wheel, faulty torque $\boldsymbol{B}(t - \boldsymbol{T}_f^o)\boldsymbol{u}_f$ is a function of the rotor speed of a reaction wheel. Thus, the time derivative of $\boldsymbol{B}(t - \boldsymbol{T}_f^o)\boldsymbol{u}_f$ is a function of the acceleration of the rotor. Due to a physical limitation, this acceleration is bounded and can be obtained when purchasing a reaction wheel. According to the calculation of $\boldsymbol{d}$ in [27], the time derivative of $\boldsymbol{d}$ is also bounded. It is thus reasonable to make the following assumption.

Assumption 3: Although input $\boldsymbol{u}_r$ is unknown, its amplitude is bounded by a constant $\varsigma > 0$, i.e., $\|\boldsymbol{u}_r\| \leq \varsigma$.

To reconstruct the states of system (21)–(23), a sliding-mode-observer-based reconstruction scheme is designed as

$$\dot{\hat{\boldsymbol{\xi}}}_1 = -k_r\hat{\boldsymbol{\xi}}_1 + k_r\hat{\boldsymbol{\xi}}_2 - \ell_{r1}\mathbf{sgn}(\boldsymbol{\varepsilon}_{r1}) - \ell_{r2}\boldsymbol{\varepsilon}_{r1} \tag{24}$$

$$\dot{\hat{\boldsymbol{\xi}}}_2 = -\ell_{r3}\boldsymbol{\varepsilon}_{r1} - \ell_{r4}\lfloor\boldsymbol{\xi}_v\rceil^{\frac{m_1}{n_1}} - \ell_{r5}\mathbf{sgn}(\boldsymbol{\xi}_v) \tag{25}$$

where $\boldsymbol{\xi}_v = \ell_1\mathbf{sgn}(\boldsymbol{\varepsilon}_{r1})$; $\boldsymbol{\varepsilon}_{r1} = \hat{\boldsymbol{\xi}}_1 - \boldsymbol{y}_r$; $\ell_{ri}, i \in \{1,2,3,4,5\}$, are gains; and m_1 and n_1 are positive odd integers such that $m_1 < n_1$.

Reconstruction error $\boldsymbol{\varepsilon}_r = [\boldsymbol{\varepsilon}_{r1}^T\ \boldsymbol{\varepsilon}_{r2}^T]^T$, with $\boldsymbol{\varepsilon}_{r2} = \hat{\boldsymbol{\xi}}_2 - \boldsymbol{\xi}_2$, is defined to examine the performance of that reconstruction module. Subtracting (21) and (22) from (24) and (25) results in the dynamics of error $\boldsymbol{\varepsilon}_r$ as follows:

$$\dot{\boldsymbol{\varepsilon}}_{r1} = -k_r\boldsymbol{\varepsilon}_{r1} + k_r\boldsymbol{\varepsilon}_{r2} - \ell_{r1}\mathbf{sgn}(\boldsymbol{\varepsilon}_{r1}) - \ell_{r2}\boldsymbol{\varepsilon}_{r1} \tag{26}$$

$$\dot{\boldsymbol{\varepsilon}}_{r2} = -\ell_{r3}\boldsymbol{\varepsilon}_{r1} - \ell_{r4}\lfloor\boldsymbol{\xi}_v\rceil^{\frac{m_1}{n_1}} - \ell_{r5}\mathbf{sgn}(\boldsymbol{\xi}_v) - \boldsymbol{u}_r. \tag{27}$$

Because the fault reconstruction module is started at $t = t_0 + 3O_T$, although it is not applied for $t < t_0 + 3O_T$, it follows from (19) that $\boldsymbol{\xi}_1(t_0 + 3O_T) = -k_r\boldsymbol{J}_g(t_0 + 3O_T)$. It leads to $\boldsymbol{\xi}_2(t_0 + 3O_T) = -\boldsymbol{F}^T(t_0 + 3O_T)\boldsymbol{d}(t_0 + 3O_T)$.

Lemma 1: Choose the initial values of observer (24) and (25) as $\hat{\boldsymbol{\xi}}_1(t_0 + 3O_T) = -k_r\boldsymbol{J}_g(t_0 + 3O_T)$ and $\hat{\boldsymbol{\xi}}_2(t_0 + 3O_T) = \mathbf{0}$; then, signal $\boldsymbol{\varepsilon}_r$ in reconstruction error system (26) and (27) is uniformly ultimately bounded.

Proof: See the Appendix.

Theorem 2: Starting at $t_0 + 3O_T$, with the application of fault reconstruction scheme (24) and (25), choose k_r and ℓ_{ri}, $i = 1,2,3,4,5$, such that

$$\ell_{r1} > \max\left\{\begin{array}{c}\left(\frac{\sqrt{3}k_r\ell_{r4}+\sqrt{3}\ell_{r5}+\varsigma}{\lambda_{\min}(\boldsymbol{M})} + \delta_1\right)^{\frac{n_1}{(n_1-m_1)}} \\ \left(\frac{k_r(\sqrt{3}\ell_{r5}+\varsigma)+\delta_1\lambda_{\min}(\boldsymbol{M})}{\sqrt{3}\ell_{r5}+\varsigma+\delta_1\lambda_{\min}(\boldsymbol{M})}\right)^{\frac{n_1}{m_1}}\end{array}\right\} \tag{28}$$

$$\ell_{r5}k_r - \varsigma > 0 \tag{29}$$

$$\pi_r \le \left\|\boldsymbol{F}^T(t_0 + 3O_T)\right\| d_{\max} \tag{30}$$

where δ_1 is a positive scalar; then, $\boldsymbol{\varepsilon}_{r1} \equiv \mathbf{0}$ and $\boldsymbol{\varepsilon}_{r2} \equiv \mathbf{0}$ will be achieved in finite time. Moreover, lumped fault $\boldsymbol{u}_l$ is reconstructed by $-\boldsymbol{P}^T\hat{\boldsymbol{\xi}}_2$ in finite time.

Proof: See the Appendix.

C. Velocity-Free FTC Design

In Theorem 2, lumped fault $\boldsymbol{u}_l$ is reconstructed by $-\boldsymbol{P}^T\hat{\boldsymbol{\xi}}_2$ in finite time T_{r2}. The following theorem is thus presented to accomplish the attitude stabilization maneuver.

Theorem 3: Consider satellite attitude model (8)–(10) with actuator faults (11), observer (16) and (17), and fault reconstruction scheme (24) and (25). Let the commanded control $\boldsymbol{u}_n$ be designed as

$$\begin{aligned}\boldsymbol{u}_n = &-k_{c1}\boldsymbol{D}^\dagger\left[\boldsymbol{e} + k_{c2}\boldsymbol{P}^T\mathbf{tanh}(\boldsymbol{\mu} + k_{c2}\boldsymbol{e})\right] \\ &+ \boldsymbol{D}^\dagger\left(\boldsymbol{R}(\boldsymbol{Q}_e)\boldsymbol{\omega}_{oi}\right)^\times\boldsymbol{J}\boldsymbol{R}(\boldsymbol{Q}_e)\boldsymbol{\omega}_{oi} + \boldsymbol{D}^\dagger\boldsymbol{P}^T\hat{\boldsymbol{\xi}}_2\end{aligned} \tag{31}$$

$$\dot{\boldsymbol{\mu}} = -k_{c3}\mathbf{tanh}(\boldsymbol{\mu} + k_{c2}\boldsymbol{e}) \tag{32}$$

where $\boldsymbol{\mu} = [\mu_1\ \mu_2\ \mu_3]^T \in \Re^3$, and k_{ci}, $i = 1,2,3$, are positive gains. Then, the satellite attitude is asymptotically stabilized, i.e., $\boldsymbol{e} \to \mathbf{0}$, $e_0 \to 1$, $\boldsymbol{\omega}_{bo} \to \mathbf{0}$, and $\boldsymbol{\Theta} \to \mathbf{0}$. Furthermore, the reaction wheel saturation problem is solved with the control torque bounded by $|u_i| \le u_{\max}$, $i = 1,2,3,4$, provided that control gains k_{c1} and k_{c2} are chosen such that

$$\begin{aligned}\|\underline{\boldsymbol{D}}_i\|\left[k_{c1}(1 + k_{c2}) + \omega_0^2\|\boldsymbol{J}\| + d_{\max}\right. \\ \left. + \left\|\boldsymbol{F}^T(t_0 + 3O_T)\right\| d_{\max}\right] \le u_{\max}.\end{aligned} \tag{33}$$

Proof: See the Appendix.

From the discussion following (A19) in the proof of Theorem 3, it is seen that $\boldsymbol{\mu}$ is used to guarantee the stability of the closed-loop system by the proposed control but without the angular velocity measurement. With the application of $\boldsymbol{\mu}$ and the proposed controller, it is obtained that $\dot{V}_c \to 0$, $\dot{\boldsymbol{\mu}} \to \mathbf{0}$, and $\ddot{\boldsymbol{\mu}} \to \mathbf{0}$. Then, it follows that $\dot{\boldsymbol{e}} \to \mathbf{0}$ from (32), and $\boldsymbol{\omega}_e \to \mathbf{0}$ from (9). This is why $\boldsymbol{\mu}$ is incorporated in controller (31).

A sufficient condition is implicitly imposed in Theorem 3 for the proposed attitude controller. That is, when a reaction wheel undergoes faults, the combined torque generated by the remaining reaction wheels is sufficient enough to compensate for those faults and external disturbances, and to achieve three-axis attitude stabilization control. It means that the combined torque is still able to achieve robust control with respect to disturbances and reliable control with respect to reaction wheel faults. Otherwise, the *three-axis attitude stabilization maneuver will never be accomplished with any control approach in literature*. At this time, the satellite becomes underactuated, but it is not the main issue to be investigated in this paper.

V. Simulation Results

As the initial step toward final experimental verification, the performance of the proposed control scheme is first numerically simulated. Non–gyroscopic attitude sensors are equipped to measure attitude angle $\boldsymbol{\Theta}$. Attitude sensors are modeled by a zero-mean Gaussian white-noise process with standard deviation $\sigma_{\text{ST}} = 35$. To obtain a high-accuracy attitude measurement, an extended Kalman filter is used in attitude determination.

Because observers (16) and (17) and (24) and (25), as well as controller (31), are inherently nonlinear, there does not exist a systematic or standard procedure to choose their gain values such as the traditional proportional–integral–derivative controller. Hence, these gains are chosen by trial and error until good performance is obtained. On the other hand, as shown in the proof of Theorem 1, larger λ_{o1} and λ_{o2} will lead to smaller T_{o1} and T_{o2}, as obtained from observer (16) and (17). As shown in the proof of Theorem 2, different gains in reconstruction scheme (24) and (25) will result in different finite times T_{r1} and T_{r2}. In addition, as shown in the proof of Theorem 3, different values of the control gains in controller (31) will lead to a different convergence time of the closed-loop attitude system, and these may also result in the different behavior of the control torque. Consequently, the gains for controller (31) are chosen as $k_{c1} = 0.01$, $k_{c2} = 0.05$, and $k_{c3} = 1.5$. The gains of observer (16) and (17) and sliding-mode observer (24) and

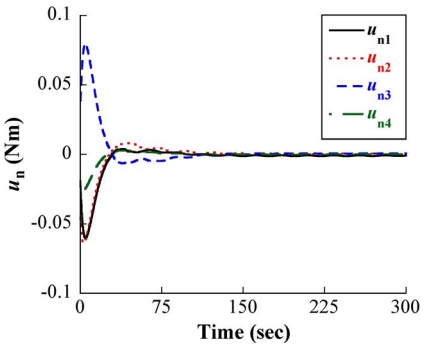

Fig. 4. Commanded control input.

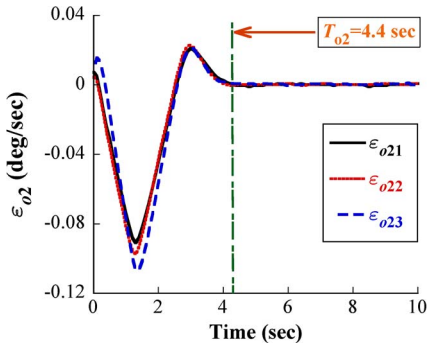

Fig. 5. Observer error ε_{o2}.

(25) are chosen as $\lambda_{o1} = 0.75$, $\lambda_{o2} = 6.5$, $\ell_{r1} = 0.15$, $\ell_{r2} = 0.05$, $\ell_{r3} = 0.5$, $\ell_{r4} = \ell_{r5} = 0.00005$, $m_1 = 19$, $n_1 = 21$, and $k_r = 0.15$.

The initial attitude angles in the simulation are randomly chosen in intervals $-0.5^\circ \le \psi(0) \le 0.5^\circ$, $-0.5^\circ \le \phi(0) \le 0.5^\circ$, and $-0.5^\circ \le \theta(0) \le 0.5^\circ$, respectively. The corresponding quaternion is $\boldsymbol{e} = [-0.000966 \;\; 0.000552 \;\; -0.000801]^T$, whereas the initial velocity is $\boldsymbol{\omega}_{bo}(0) = [0.5702 \;\; 0.2467 \;\; -0.4887]^\circ/\text{s}$.

A. Reaction Wheel Fault Scenarios

The reaction wheel mounted in line with the $+X$-axis loses 20% power when the attitude maneuver begins, i.e., $T_{f1}^o = 0$, $a_1 = 20$, and $u_{f1} = -0.2u_{n1}$. The actuator mounted in line with the $+Y$-axis (wheel no. 2) loses its 45% power in the time interval between 4 and 10 s. Moreover, the continuous generation of the reaction torque fault with a value of -0.025 N $\cdot$ m will immediately occur, i.e., $a_4 = \infty$, and

$$\boldsymbol{u}_{f2} = \begin{cases} -0.45u_{n2}, & \text{if } 4 \le t \le 10 \\ -0.025, & \text{if } t > 10. \end{cases} \tag{34}$$

The wheel fixed in line with the $+Z$-axis (wheel no. 3) totally fails after 15 s, i.e., $u_{f3} = -u_{n3}$, $T_{f3}^o = 15$, and $a_3 = 150$. In addition, the redundant wheel (wheel no. 4) decreases 90% of its torque after 8 s, i.e., $u_{f4} = -0.9u_{n4}$, $T_{f4}^o = 8$, and $a_3 = 75$.

B. System Responses

When the reaction wheels undergo the aforementioned faults, with the application of the proposed velocity-free fault-tolerant attitude stabilization control scheme (named as VFTASC), Figs. 4–8 illustrate its attitude control performance. It is interesting to see that the actuator saturation problem is addressed by the proposed scheme as the commanded control shown in Fig. 4. As shown in Fig. 5, the estimation error $\boldsymbol{\varepsilon}_{o2}$ of the sliding-mode observer for the immeasurable angular velocity $\boldsymbol{\omega}_{bi}$ (or $\dot{\boldsymbol{\Theta}}$) will converge to zero in a finite time of 4.4 s, i.e., $T_{O2} = 4.4$. This successfully verifies the conclusion in Theorem 1 that the sliding observer state $\hat{\boldsymbol{x}}_2$ can estimate state $\boldsymbol{x}_2$ with zero error in finite time.

Fig. 6 shows the successful fault reconstruction using the incorporated reconstruction scheme (26) and (27). It is shown in Fig. 6(a) that accurate reconstruction is achieved within 100 s.

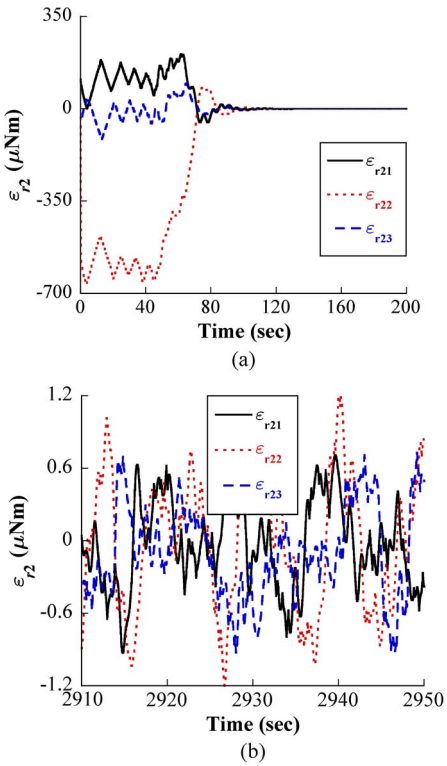

Fig. 6. Fault reconstruction error ε_{r2}. (a) Initial response. (b) Steady-state behavior.

This validates the result in Theorem 2. Moreover, as shown by the steady-state behavior of ε_{r2} in Fig. 6, the accuracy of the reconstruction for $\boldsymbol{u}_l$ is smaller than 1.2×10^{-6} N $\cdot$ m. Due to the accurate reconstruction of the reaction wheel faults and external disturbances supplied by scheme (26) and (27), controller (31) can completely compensate for the effects of actuator faults and reject external disturbances. The controller thus produces the asymptotic stabilization of the angular velocity and the attitude.

Although the angular velocity measurement is not used to implement the proposed controller, the satellite's actual angular velocity is still shown in Fig. 7, whereas the unit attitude quaternion is presented in Fig. 8. As the steady-state behavior in Figs. 7 and 8 shows, the attitude pointing accuracy achieves an $|e_i| \le 4.0 \times 10^{-5}$ level that corresponds to the attitude angles $\boldsymbol{\Theta}$ that are less than 0.005°, and the attitude stability is within $0.001^\circ/\text{s}$. Therefore, the attitude stability and the pointing accuracy satisfy a set of stringent pointing requirements for

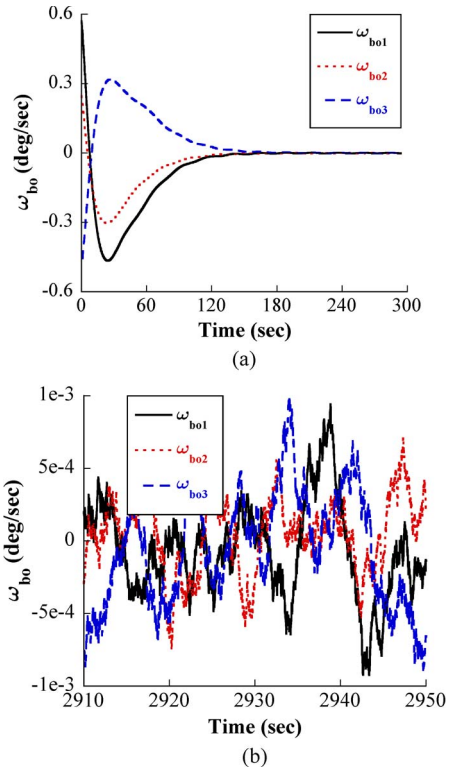

Fig. 7. Angular velocity of the satellite. (a) Initial response. (b) Steady-state behavior.

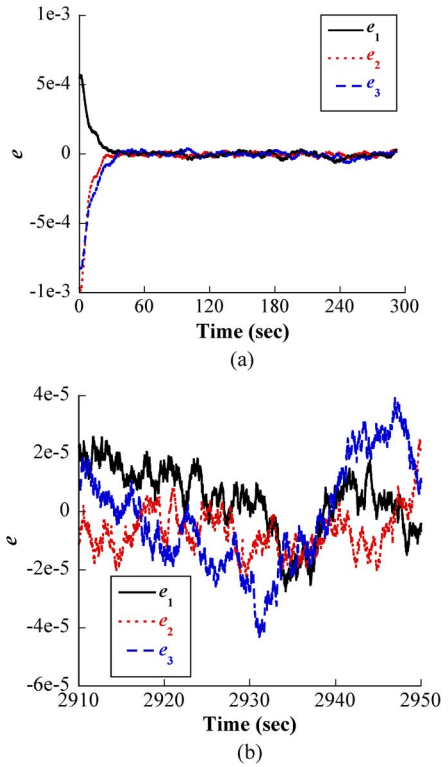

Fig. 8. Unit attitude quaternion of the satellite. (a) Initial response. (b) Steady-state behavior.

downloading image data to a ground station in the face of faults and disturbances, and the considered communication mission is thus considered successfully accomplished.

C. Quantitative Analysis

The results are further compared with the unit-quaternion-based output feedback control (UQOFC) [17] and the terminal sliding-mode-based velocity-free controller (TSMOBVFC) [28]. Both the TSMOBVFC and the UQOFC do not require the angular velocity measurement to implement their controllers. The simulation in the absence of actuator faults is also carried out to further validate the effectiveness of the proposed approach. In assessing the performance of these three schemes, two important criteria should be considered, i.e., the average consumption of energy (P_E) and the percentage of successfully accomplished missions (P_m) with respect to the planned mission, as follows:

$$P_E = \frac{1}{T_{\text{total}}} \int_0^{T_{\text{total}}} \|\boldsymbol{u}_n(t)\|^2 \, dt \quad P_m = \frac{T_{\text{successfully}}}{T_{\text{total}}} \times 100\%.$$

These two indexes quantitatively state how efficient the controller is. Here, T_{total} denotes the attitude maneuver's time period. It is chosen as $T_{\text{total}} = 0.5O_T = 2946.8$ s according to the attitude stabilization mission in Section II-B. $T_{\text{successfully}}$ denotes the sum of the time period during which the attitude pointing accuracy is within $0.005°$, and its stability is within $0.0012°/\text{s}$. $T_{\text{successfully}}$ is very crucial and is to be minimized so that data downloading is able to be carried out in the few tens of seconds during the period of a typical satellite passing over a ground tracking station. The larger $T_{\text{successfully}}$ is, the more image data can be downloaded. In addition, the larger P_E is, the more energy is consumed during the attitude stabilization maneuver. These two indexes are the worst affected during actuator failures and thus degrade the performance of the mission to a significant extent.

In the absence or presence of reaction wheel faults, the corresponding performance of index P_E and that of index P_m are shown in Figs. 9 and 10, respectively. The following are found.

1) When all actuators run normally, although the TSMOBVFC can achieve the same value P_m [as shown in Fig. 9(a)] as the VFTASC by tuning the gains of the TSMOBVFC, the index value P_E that was obtained from the TSMOBVFC is larger than that from the VFTASC. That is because, although the TSMOBVFC is able to handle actuator saturation and external disturbances as the VFTASC, it is actually a robust control scheme; hence, its controller has certain conservativeness. Due to control term $\boldsymbol{D}^{\dagger}\boldsymbol{P}^T\hat{\boldsymbol{\xi}}_2$ in (31), the VFTASC can compensate for the external disturbance in real time, and its conservativeness is thus much weaker. On the other hand, when reaction wheels undergo faults, the index value P_m from the TSMOBVFC is less than that from the VFTASC. This can be seen in Fig. 10(a). That is because the TSMOBVFC can only handle partial loss of control power, but it is unable to handle the fault type occurring in the no. 2 wheel.
2) Because the UQOFC is only able to solve the attitude stabilization problem of the satellite subject to actuator saturation, the satellite should be free of external disturbances. As a result, when reaction wheels are healthy,

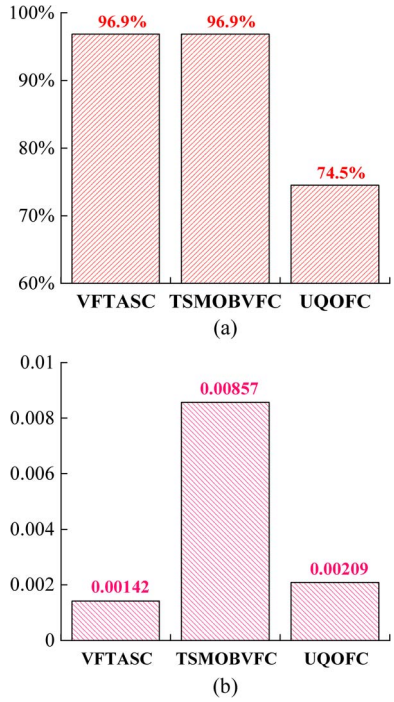

Fig. 9. Indexes P_m and P_E in the absence of reaction wheel faults. (a) P_m. (b) P_E.

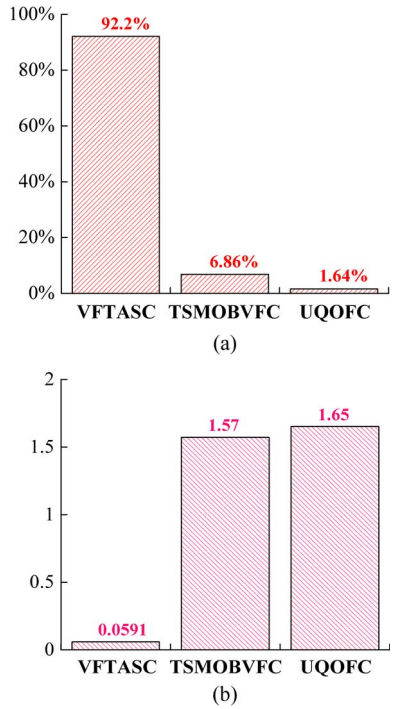

Fig. 10. Indexes P_m and P_E in the case of reaction wheel faults. (a) P_m. (b) P_E.

due to the external disturbances, the UQOFC will achieve a smaller P_m than the VFTASC and the TSMOBVFC, i.e., $P_m = 74.5\%$. That is because the VFTASC and the TSMOBVFC are capable of eliminating the effect of external disturbances on the control accuracy. Additionally, because the UQOFC has no capability to tolerate actuator faults, a quite small P_m, i.e., $P_m = 1.64\%$, is obtained in the presence of faults. That can be seen in Fig. 10(a).

3) In the presence of actuator faults, both the TSMOBVFC and the UQOFC consumed more energy than the VTFASC, as can be seen in Fig. 10(b). That is because the TSMOBVFC and the UQOFC were not able to handle the fault in the no. 2 reaction wheel. When that type of fault occurred, the TSMOBVFC and the UQOFC would continue issuing the maneuvering control command that may no longer be achievable by the system in spite of the occurrence of the fault. Under this situation, the required control effort will quickly saturate the actuators while striving to maintain the "healthy" maneuvering performance. Consequently, much more energy was consumed.

Based on the comparisons of P_E and P_m in Figs. 9 and 10, it is seen that, whether faults occur or not, the proposed control approach provides better performance than the controllers presented in [17] and [28]. The proposed solution maintains good attitude control under both normal and fault conditions, and it provides higher pointing accuracy to guarantee the satellite to download much more image data and thus accomplishes the planned mission as much as possible.

VI. Conclusion and Future Work

A fault-tolerant attitude stabilization control without angular velocity measurement was presented. The closed-loop attitude system was asymptotically stabilized in the presence of external disturbances and reaction wheel faults. The problem of actuator saturation was solved. The controller provided the satellite attitude stabilization system design with a low-cost solution, in which only attitude sensors are required and rate sensors and magnetic torquers are not required. Under both faulty and fault-free cases, the proposed control scheme provides significantly better performance compared with two existing controllers in terms of the performance index percentage of successfully accomplished missions. Although the proposed controller was able to tolerate reaction wheel faults, it did not consider the problem of energy consumption in the controller design. Hence, as one of future works, it is desirable to design an optimal FTC by using a control allocation technique to achieve attitude control with minimum energy consumed. Moreover, it should be also noticed that the attitude model established in Section III for the attitude controller design does not consider issues such as uncertainty, modeling, and measurement errors. These issues may affect the accuracy of the attitude model and hence should be further investigated in the future.

Appendix

A. Proof of Theorem 1

Define observer errors $\boldsymbol{\varepsilon}_{o1} = \hat{\boldsymbol{x}}_1 - \boldsymbol{x}_1$ and $\boldsymbol{\varepsilon}_{o2} = \hat{\boldsymbol{x}}_2 - \boldsymbol{x}_2$; the observer error dynamics can be obtained from (15)–(17) such that

$$\dot{\boldsymbol{\varepsilon}}_{o1} = \boldsymbol{\varepsilon}_{o2} - \lambda_{o1}\mathbf{sgn}(\boldsymbol{\varepsilon}_{o1}) \tag{A1}$$

$$\dot{\boldsymbol{\varepsilon}}_{o2} = \Delta \boldsymbol{g}_4(x_2, \hat{x}_2) - \boldsymbol{J}^{-1}\boldsymbol{K}\boldsymbol{\varepsilon}_{o1} - \boldsymbol{J}^{-1}\boldsymbol{D}\boldsymbol{B}(t - T_0)\boldsymbol{u}_f + \delta_o\left(\lambda_{o2}\mathbf{sgn}(\tilde{\boldsymbol{x}}_2 - \hat{\boldsymbol{x}}_2)\right) \tag{A2}$$

where $\Delta \boldsymbol{g}_4(x_2, \hat{x}_2) = \boldsymbol{J}^{-1}[\boldsymbol{C}\boldsymbol{x}_2 - \boldsymbol{C}\hat{\boldsymbol{x}}_2 - (\boldsymbol{d} - \Delta \boldsymbol{g}_2 - \Delta \boldsymbol{g}_3)]$.

Consider a candidate Lyapunov function as $V_{o1}=0.5\boldsymbol{\varepsilon}_{o1}^T\boldsymbol{\varepsilon}_{o1}$. It then follows from (A1) that $\dot{V}_{o1}\le-\|\boldsymbol{\varepsilon}_{o1}\|(\lambda_{o1}-\|\boldsymbol{\varepsilon}_{o2}\|)$. One could choose $\lambda_{o1}>\|\boldsymbol{\varepsilon}_{o2}\|+\ell_{o1}$, with ℓ_{o1} being a positive scalar. Then, we have

$$\dot{V}_{o1}\le-\ell_{o1}\|\boldsymbol{\varepsilon}_{o1}\|=-\ell_{o1}\sqrt{2V_{o1}}. \tag{A3}$$

This ensures that $\dot{V}_{o1}<0$ for all $\|\boldsymbol{\varepsilon}_{o1}\|\neq0$ and the finite-time convergence of $\boldsymbol{\varepsilon}_{o1}$ to sliding surface $\boldsymbol{\varepsilon}_{o1}=\mathbf{0}$. Alternatively, choosing $\lambda_{o1}>\max_{t\in[t_0+2O_T,T_{o1}]}\|\boldsymbol{\varepsilon}_{o2}(t)\|$, where T_{o1} denotes the time it takes for $\boldsymbol{\varepsilon}_{o1}$ to converge to the sliding surface, allows a fixed value for λ_{o1} and ensures that $\dot{V}_{o1}<0$ for all $\|\boldsymbol{\varepsilon}_{o1}\|\neq0$. To show that the convergence of $\boldsymbol{\varepsilon}_{o1}$ to zero is achieved in T_{o1}, integrating both sides of (A3) from t_0+2O_T to t yields $\|\boldsymbol{\varepsilon}_{o1}(t)\|\le\|\boldsymbol{\varepsilon}_{o1}(t_0+2O_T)\|-\ell_{o1}[t-(t_0+2O_T)]$. Then, for all time $t\ge T_{o1}=t_0+2O_T+\|\boldsymbol{\varepsilon}_{o1}(t_0+2O_T)\|/\ell_{o1}$, $\|\boldsymbol{\varepsilon}_{o1}(t)\|\equiv0$ is obtained. $\boldsymbol{\varepsilon}_{o1}$ will reach sliding surface $\boldsymbol{\varepsilon}_{o1}=0$ by time T_{o1}. On that surface, $\boldsymbol{\varepsilon}_{o1}=\dot{\boldsymbol{\varepsilon}}_{o1}=0$, and solving for the equivalent output injection yields $(\lambda_{o1}\mathbf{sgn}(\boldsymbol{\varepsilon}_{o1}))_{\text{eq}}=\boldsymbol{\varepsilon}_{o2}$. This leads to $\tilde{\boldsymbol{x}}_2=\boldsymbol{x}_2$.

After time T_{o1}, error dynamics (A1) and (A2) have the following form:

$$\dot{\boldsymbol{\varepsilon}}_{o1}=0 \tag{A4}$$

$$\dot{\boldsymbol{\varepsilon}}_{o2}=\Delta\boldsymbol{g}_4(x_2,\hat{x}_2)-\lambda_{o2}\mathbf{sgn}(\boldsymbol{\varepsilon}_{o2})-\boldsymbol{J}^{-1}\boldsymbol{D}\left[\boldsymbol{B}(t-T_0)\boldsymbol{u}_f\right]. \tag{A5}$$

At this time, define another candidate Lyapunov function $V_{o2}=0.5\boldsymbol{\varepsilon}_{o1}^T\boldsymbol{\varepsilon}_{o1}+0.5\boldsymbol{\varepsilon}_{o2}^T\boldsymbol{\varepsilon}_{o2}$. It leaves V_{o2} from (A4) and (A5) such that

$$\dot{V}_{o2}\le-\lambda_{o2}\|\boldsymbol{\varepsilon}_{o2}\|+\boldsymbol{\varepsilon}_{o2}^T\Delta\boldsymbol{g}_4(x_2,\hat{x}_2)-\boldsymbol{\varepsilon}_{o2}^T\boldsymbol{J}^{-1}\boldsymbol{D}\left[\boldsymbol{B}(t-T_0)\boldsymbol{u}_f\right] \tag{35}$$

$$\le-\|\boldsymbol{\varepsilon}_{o2}\|\{\lambda_{o2}-\|\Delta\boldsymbol{g}_4(x_2,\hat{x}_2)\|-2\|\boldsymbol{J}^{-1}\boldsymbol{D}\|u_{\max}\}. \tag{A6}$$

Choosing $\lambda_{o2}>\|\Delta\boldsymbol{g}_4(x_2,\hat{x}_2)\|+2\|\boldsymbol{J}^{-1}\boldsymbol{D}\|u_{\max}+\ell_{o2}$, $\ell_{o2}>0$ results in $\dot{V}_{o2}\le-\ell_{o2}\|\boldsymbol{\varepsilon}_{o2}\|<0$ for all $\|\boldsymbol{\varepsilon}_{o2}\|\neq0$. This guarantees that $\boldsymbol{\varepsilon}_{o2}$ reaches sliding surface $\boldsymbol{\varepsilon}_{o2}=0$ in finite time. One can alternatively choose a fixed value for λ_{o2} as $\lambda_{o2}>\max_{t\in[T_{o1},T_{o2}]}[\|\Delta\boldsymbol{g}_4(x_2,\hat{x}_2)\|+2\|\boldsymbol{J}^{-1}\boldsymbol{D}\|u_{\max}]$, where T_{o2} is the time required for $\boldsymbol{\varepsilon}_{o2}$ to reach surface $\boldsymbol{\varepsilon}_{o2}=0$. Integrating both sides of $\dot{V}_{o2}\le-\ell_{o2}\|\boldsymbol{\varepsilon}_{o2}\|$ from T_{o1} to t yields

$$\|\boldsymbol{\varepsilon}_{o2}(t)\|\le\|\boldsymbol{\varepsilon}_{o2}(T_{o1})\|-\ell_{o2}(t-T_{o1}). \tag{A7}$$

Hence, solving (A7) yields $T_{o2}=T_{o1}+\|\boldsymbol{\varepsilon}_{o2}(T_{o1})\|/\ell_{o2}$, and $\|\boldsymbol{\varepsilon}_{o2}(t)\|\equiv0$ for all $t\ge T_{o2}$. This completes the proof. □

B. Proof of Lemma 1

Choosing a candidate Lyapunov function $V_{r1}=0.5\boldsymbol{\varepsilon}_{r1}^T\boldsymbol{\varepsilon}_{r1}+0.5\boldsymbol{\varepsilon}_{r2}^T\boldsymbol{\varepsilon}_{r2}$ for error dynamics (26) and (27), it yields

$$\begin{aligned}\dot{V}_{r1}&=-k_r\boldsymbol{\varepsilon}_{r1}^T\boldsymbol{\varepsilon}_{r1}+k_r\boldsymbol{\varepsilon}_{r1}^T\boldsymbol{\varepsilon}_{r2}-\ell_{r1}\boldsymbol{\varepsilon}_{r1}^T\mathbf{sgn}(\boldsymbol{\varepsilon}_{r1})-\ell_{r2}\boldsymbol{\varepsilon}_{r1}^T\boldsymbol{\varepsilon}_{r1}\\&\quad-\ell_{r3}\boldsymbol{\varepsilon}_{r2}^T\boldsymbol{\varepsilon}_{r1}-\ell_{r4}\boldsymbol{\varepsilon}_{r2}^T\lfloor\boldsymbol{\xi}_v\rceil^{\frac{m_1}{n_1}}-\ell_{r5}\boldsymbol{\varepsilon}_{r2}^T\mathbf{sgn}(\boldsymbol{\xi}_v)-\boldsymbol{\varepsilon}_{r2}^T\boldsymbol{u}_r\\&\le\left(\sqrt{3}\ell_{r4}\ell_{r1}^{\frac{m_1}{n_1}}+\sqrt{3}\ell_{r5}+\varsigma\right)\|\boldsymbol{\varepsilon}_r\|-\boldsymbol{\varepsilon}_r^T\boldsymbol{M}\boldsymbol{\varepsilon}_r-\ell_{r1}\|\boldsymbol{\varepsilon}_{r1}\|\end{aligned} \tag{A8}$$

where $\boldsymbol{M}=\begin{bmatrix}(k_r+\ell_{r2})\boldsymbol{I}_3 & -k_r\boldsymbol{I}_3\\ \ell_{r3}\boldsymbol{I}_3 & \mathbf{0}\end{bmatrix}$. Because k_r, ℓ_{r2}, and ℓ_{r3} are positive, $\boldsymbol{M}$ is positive definite, and $\lambda_{\min}(\boldsymbol{M})>0$. Furthermore, we have

$$\begin{aligned}\dot{V}_{r1}&\le-\lambda_{\min}(\boldsymbol{M})\|\boldsymbol{\varepsilon}_r\|^2+\left(\sqrt{3}\ell_{r4}\ell_{r1}^{\frac{m_1}{n_1}}+\sqrt{3}\ell_{r5}+\varsigma\right)\|\boldsymbol{\varepsilon}_r\|\\&=-\|\boldsymbol{\varepsilon}_r\|\left[\lambda_{\min}(\boldsymbol{M})\|\boldsymbol{\varepsilon}_r\|-\left(\sqrt{3}\ell_{r4}\ell_{r1}^{\frac{m_1}{n_1}}+\sqrt{3}\ell_{r5}+\varsigma\right)\right].\end{aligned} \tag{A9}$$

If $\boldsymbol{\varepsilon}_r$ is outside compact set $\mathcal{D}=\{\boldsymbol{\varepsilon}_r:\|\boldsymbol{\varepsilon}_r\|\le\pi_r\}$, where $\pi_r=(\sqrt{3}\ell_{r4}\ell_{r1}^{m_1/n_1}+\sqrt{3}\ell_{r5}+\varsigma)/\lambda_{\min}(\boldsymbol{M})$, then $\dot{V}_{r1}<0$, and $\|\boldsymbol{\varepsilon}_r\|$ will decrease monotonically. A decreasing value of V_{r1} eventually drives $\boldsymbol{\varepsilon}_r$ into set $\mathcal{D}$ in finite time, and it will never go outside of $\mathcal{D}$. Set $\mathcal{D}$ is thus attractive. According to the Lyapunov theory and the LaSalle extension, $\boldsymbol{\varepsilon}_r$ is concluded to be uniformly ultimately bounded. Furthermore, it is obtained from the initial values of $\hat{\boldsymbol{\xi}}_1$ and $\hat{\boldsymbol{\xi}}_2$ that

$$\begin{aligned}\|\boldsymbol{\varepsilon}_r(t_0+3O_T)\|&=\|\boldsymbol{\xi}_2(t_0+3O_T)\|\\&=\left\|\boldsymbol{F}^T(t_0+3O_T)\boldsymbol{d}(t_0+3O_T)\right\|\\&\le\left\|\boldsymbol{F}^T(t_0+3O_T)\right\|d_{\max}.\end{aligned} \tag{A10}$$

Then, $\|\boldsymbol{\varepsilon}_r\|\le\max\{\pi_r,\|\boldsymbol{F}^T(t_0+3O_T)\|d_{\max}\}$ is guaranteed for all $t\ge t_0+3O_T$. □

C. Proof of Theorem 2

The proof uses the Lyapunov stability theory and is separated into two parts as follows.

1) Finite-Time Convergence of $\boldsymbol{\varepsilon}_{r1}$: Consider a Lyapunov function $V_{r2}=0.5\boldsymbol{\varepsilon}_{r1}^T\boldsymbol{\varepsilon}_{r1}$; it is obtained from (26) that

$$\dot{V}_{r2}\le-(k_r+\ell_{r2})\|\boldsymbol{\varepsilon}_{r1}\|^2-(\ell_{r1}-k_r\|\boldsymbol{\varepsilon}_{r2}\|)\|\boldsymbol{\varepsilon}_{r1}\|. \tag{A11}$$

Rearranging $\ell_{r1}>[\delta_1+(\sqrt{3}k_r\ell_{r4}+\sqrt{3}\ell_{r5}+\varsigma)/\lambda_{\min}(\boldsymbol{M})]^{n_1/(n_1-m_1)}$ and $\ell_{r1}>((k_r(\sqrt{3}\ell_{r5}+\varsigma)+\delta_1\lambda_{\min}(\boldsymbol{M}))/(\sqrt{3}\ell_{r5}+\varsigma+\delta_1\lambda_{\min}(\boldsymbol{M})))^{n_1/m_1}$ in (28) yields

$$\begin{aligned}\ell_{r1}&>\frac{\sqrt{3}k_r\ell_{r4}\ell_{r1}^{\frac{m_1}{n_1}}+(\sqrt{3}\ell_{r5}+\varsigma)\ell_{r1}^{\frac{m_1}{n_1}}}{\lambda_{\min}(\boldsymbol{M})}+\delta_1\ell_{r1}^{\frac{m_1}{n_1}}\\&>\frac{k_r\ell_{r4}\ell_{r1}^{\frac{m_1}{n_1}}\sqrt{3}+k_r(\sqrt{3}\ell_{r5}+\varsigma)}{\lambda_{\min}(\boldsymbol{M})}+\delta_1=k_r\pi_r+\delta_1.\end{aligned} \tag{A12}$$

From Lemma 1 and (12), one has $\ell_{r1}-k_r\|\boldsymbol{\varepsilon}_{r2}\|>\delta_1$ in finite time, and

$$\dot{V}_{r2}<-\delta_1\|\boldsymbol{\varepsilon}_{r1}\|=-\delta_1\sqrt{2V_{r2}}<0 \tag{A13}$$

for $\|\boldsymbol{\varepsilon}_{r1}\|\neq0$. Integrating both sides of (A13) from t_0+3O_T to t yields $\|\boldsymbol{\varepsilon}_{r1}(t)\|\le\|\boldsymbol{\varepsilon}_{r1}(t_0+3O_T)\|-\delta_1[t-(t_0+3O_T)]$, and $\boldsymbol{\varepsilon}_{r1}(t)\equiv\mathbf{0}$ for $t\ge T_{r1}=t_0+3O_T+\|\boldsymbol{\varepsilon}_{r1}(t_0+3O_T)\|/\delta_1$. It is thus concluded that error state $\boldsymbol{\varepsilon}_{r1}$ reaches sliding surface $\boldsymbol{\varepsilon}_{r1}=\dot{\boldsymbol{\varepsilon}}_{r1}=\mathbf{0}$ in finite time T_{r1}. Moreover, by time $t=T_{r1}$, solving for the equivalent output injection yields

$$(\boldsymbol{\xi}_v)_{\text{eq}}=(\ell_{r1}\mathbf{sgn}(\boldsymbol{\varepsilon}_{r1}))_{\text{eq}}=k_r\boldsymbol{\varepsilon}_{r2}. \tag{A14}$$

2) Finite-Time Convergence of ε_{r2}: After time T_{r1}, substituting $\varepsilon_{r1} = \dot{\varepsilon}_{r1} = \mathbf{0}$ and (A14) into (27) yields

$$\dot{\varepsilon}_{r2} = -\ell_{r4}\lfloor k_r\varepsilon_{r2}\rceil^{\frac{m_1}{n_1}} - \ell_{r5}\mathbf{sgn}(k_r\varepsilon_{r2}) - \boldsymbol{u}_r. \tag{A15}$$

Define another Lyapunov function as $V_{r3} = 0.5\varepsilon_{r2}^T\varepsilon_{r2}$. With (A15) and (29), one has

$$\begin{aligned}\dot{V}_{r3} &= \varepsilon_{r2}^T\left(-\ell_{r4}k_r^{\frac{m_1}{n_1}}\lfloor\varepsilon_{r2}\rceil^{\frac{m_1}{n_1}} - \ell_{r5}\mathbf{sgn}(k_r\varepsilon_{r2}) - \boldsymbol{u}_r\right)\\ &\le -\ell_{r4}k_r^{\frac{m_1}{n_1}}\|\varepsilon_{r2}\|^{\frac{(m_1+n_1)}{n_1}} - (\ell_{r5}k_r - \zeta)\|\varepsilon_{r2}\|\\ &< -\ell_{r4}k_r^{\frac{m_1}{n_1}}2^{\frac{(m_1+n_1)}{(2n_1)}}V_{r3}^{\frac{(m_1+n_1)}{(2n_1)}}.\end{aligned} \tag{A16}$$

Because m_1 and n_1 are odd, m_1+n_1 is always even. Using $V_{r2}^{m_1+n_1/2n_1} > 0$ and solving (A16) leads to $V_{r2}(t) \equiv 0$ for $t \ge T_{r2} = (2^{(n_1-m_1)/(2n_1)}n_1V_{r2}^{(n_1-m_1)/(2n_1)}(T_{r1}))/(\ell_{r4}k_r^{m_1/n_1}(n_1-m_1)) + T_{r1}$. Accordingly, it is found that $\varepsilon_{r2}(t) \equiv \mathbf{0}$ for all $t \ge T_{r2}$.

With the definition of ε_{r2} and $\bar{\boldsymbol{\tau}}_l$, one has $\bar{\boldsymbol{\tau}}_l(t) \equiv \hat{\boldsymbol{\xi}}_2(t)$, and $\boldsymbol{u}_l(t) \equiv -\boldsymbol{P}^T\bar{\boldsymbol{\tau}}_l(t) \equiv -\boldsymbol{P}^T\hat{\boldsymbol{\xi}}_2(t)$ for $t \ge T_{r2}$. $\boldsymbol{u}_l$ is thus reconstructed by $\boldsymbol{P}^T\hat{\boldsymbol{\xi}}_2$ in finite time T_{r2}. □

D. Proof of Theorem 3

The proof is separated into two parts as follows.

1) Stability Analysis of Closed-Loop System: Consider the following radially unbounded positive-definite Lyapunov function candidate for the system:

$$V_c = \frac{\boldsymbol{\omega}_{bo}^T\boldsymbol{J}\boldsymbol{\omega}_{bo}}{2k_{cl}} + \boldsymbol{e}^T\boldsymbol{e} + (1-e_0)^2 + \sum_{i=1}^{3}\ln\left(\cosh(\mu_i + k_{c2}e_i)\right). \tag{A17}$$

Using (8)–(10) and (31) and (32), one obtains

$$\dot{V}_c = \frac{\boldsymbol{\omega}_{bo}^T}{k_{c1}}\left(\boldsymbol{P}^T\hat{\boldsymbol{\xi}}_2 + \boldsymbol{u}_l\right) - \dot{\boldsymbol{\mu}}^T\mathbf{tanh}\left(\frac{\dot{\boldsymbol{\mu}}}{k_{c3}}\right). \tag{A18}$$

Applying the reconstruction module leads to $\boldsymbol{u}_l \equiv -\boldsymbol{P}^T\hat{\boldsymbol{\xi}}_2$ for all $t \ge t_{r2}$. Thereby, after time T_{r2}, it leaves (A18) as

$$\dot{V}_c = -\dot{\boldsymbol{\mu}}^T\mathbf{tanh}\left(\frac{\dot{\boldsymbol{\mu}}}{k_{c3}}\right) \le -k_{c3}\|\mathbf{tanh}\left(\frac{\dot{\boldsymbol{\mu}}}{k_{c3}}\right)\|^2 \le 0 \tag{A19}$$

which is a negative semidefinite decrescent function. Because the attitude stabilization maneuver is started at t_s, (A19) leads to $\int_{t_s}^{\infty}\dot{V}_c dt \le V_c(t_s) - V_c(\infty) < \infty$, and since V_c is radially unbounded, all the solutions are bounded. Hence, noting that $\dot{V}_c$ is uniformly continuous by invoking Barbalat's lemma, one has $\lim_{t\to\infty}\dot{V}_c(t) = 0$. Using the uniform continuity of $\dot{V}_c$ results in $\lim_{t\to\infty}\ddot{V}_c(t) = 0$. Then, it follows that $\lim_{t\to\infty}\dot{\boldsymbol{\mu}}(t) = \lim_{t\to\infty}\ddot{\boldsymbol{\mu}}(t) = 0$, and $\lim_{t\to\infty}\dot{\boldsymbol{e}}(t) = \mathbf{0}$ from (32). From (9), $\lim_{t\to\infty}\boldsymbol{\omega}_e(t) = \mathbf{0}$ is thus obtained because the nonsingularity of $\boldsymbol{P}(\boldsymbol{Q}_e)$ is guaranteed. It is finally calculated from those results, i.e., $\boldsymbol{u}_l(t) \equiv -\boldsymbol{P}^T\hat{\boldsymbol{\xi}}_2(t)$ for $t \ge T_{r2}$, (10), and (31), that $\lim_{t\to\infty}\boldsymbol{e}(t) = \mathbf{0}$. This implies that $\lim_{t\to\infty}e_0(t) = \pm 1$.

Because $\boldsymbol{Q}_e = [1\ \mathbf{0}]^T$ and $\boldsymbol{Q}_e = [-1\ \mathbf{0}]^T$ denote the same equilibrium point in the physical space, they yield the same attitude rotation matrix $\boldsymbol{R}(\boldsymbol{Q}_e)$. However, only $\boldsymbol{Q}_e = [1\ \mathbf{0}]^T$ is an attractive equilibrium point, and $\boldsymbol{Q}_e = [-1\ \mathbf{0}]^T$ is not an attractor but a repeller equilibrium [17]. One can conclude that the equilibrium point of the closed-loop system is asymptotically stable. Using the algebraic relationship shown in (7), it leads $\lim_{t\to\infty}\boldsymbol{Q}_e(t) = [1\ \mathbf{0}]^T$ to $\lim_{t\to\infty}\boldsymbol{\Theta}(t) = \mathbf{0}$.

2) Analysis of Designed Control Torque's Upper Bound: From (11) and controller (31), one has

$$\begin{aligned}\boldsymbol{u} = &-\boldsymbol{D}^\dagger\boldsymbol{d} - k_{c1}\boldsymbol{D}^\dagger\left[\boldsymbol{e} + k_{c2}\boldsymbol{P}^T\mathbf{tanh}(\boldsymbol{\mu} + k_{c2}\boldsymbol{e})\right]\\ &+ \boldsymbol{D}^\dagger\boldsymbol{u}_l + \boldsymbol{D}^\dagger\left(\boldsymbol{R}(\boldsymbol{Q}_e)\boldsymbol{\omega}_{oi}\right)^\times\boldsymbol{J}\boldsymbol{R}(Q_e)\boldsymbol{\omega}_{oi} + \boldsymbol{D}^\dagger\boldsymbol{P}^T\hat{\boldsymbol{\xi}}_2.\end{aligned} \tag{A20}$$

Using $\|\boldsymbol{R}(\boldsymbol{Q}_e)\| = 1$, $\|\boldsymbol{P}\| = 1$, and $\|\mathbf{tanh}(\boldsymbol{a})\| \le 1$ for all $\boldsymbol{a}$, the actual output torque of each reaction wheel can be calculated as

$$\begin{aligned}|u_i| &= -k_{c1}\underline{\boldsymbol{D}}_i\left[\boldsymbol{e} + k_{c2}\boldsymbol{P}^T\mathbf{tanh}(\boldsymbol{\mu} + k_{c2}\boldsymbol{e})\right]\\ &\quad + \underline{\boldsymbol{D}}_i\left(\boldsymbol{R}(\boldsymbol{Q}_e)\boldsymbol{\omega}_{oi}\right)^\times\boldsymbol{J}\boldsymbol{R}(\boldsymbol{Q}_e)\boldsymbol{\omega}_{oi} + \underline{\boldsymbol{D}}_i\boldsymbol{P}^T\hat{\boldsymbol{\xi}}_2 + \underline{\boldsymbol{D}}_i\boldsymbol{u}_l - \underline{\boldsymbol{D}}_i\boldsymbol{d}\\ &\le k_{c1}(1+k_{c2})\|\underline{\boldsymbol{D}}_i\| + \omega_0^2\|\boldsymbol{J}\|\|\underline{\boldsymbol{D}}_i\|\\ &\quad + \|\underline{\boldsymbol{D}}_i\|d_{\max} + \underline{\boldsymbol{D}}_i\left(\boldsymbol{P}^T\hat{\boldsymbol{\xi}}_2 + \boldsymbol{u}_l\right)\end{aligned} \tag{A21}$$

where $i = 1, 2, 3, 4$, and $\underline{\boldsymbol{D}}_i$ is the ith row of matrix $\boldsymbol{D}^\dagger$.

Because it can be obtained from the reconstruction module that $\boldsymbol{u}_l(t) \equiv -\boldsymbol{P}^T\hat{\boldsymbol{\xi}}_2(t)$ for $t \ge T_{r2}$, it yields $\boldsymbol{P}^T\hat{\boldsymbol{\xi}}_2 + \boldsymbol{u}_l = \mathbf{0}$ for $t \ge T_{r2}$ and $\boldsymbol{P}^T\hat{\boldsymbol{\xi}}_2 + \boldsymbol{u}_l = \boldsymbol{P}^T\boldsymbol{\varepsilon}_{r2}(t)$ for $t < T_{r2}$. From the proof of Lemma 1 and (30), one has $\|\boldsymbol{\varepsilon}_r\| \le \|\boldsymbol{F}^T(t_0 + 3O_T)\|d_{\max}$. This leads to

$$\left\|\boldsymbol{P}^T\hat{\boldsymbol{\xi}}_2 + \boldsymbol{u}_l\right\| \le \left\|\boldsymbol{P}^T\boldsymbol{\varepsilon}_{r2}\right\| = \left\|\boldsymbol{F}^T(t_0 + 3O_T)\right\|d_{\max},\ t \ge t_s. \tag{A22}$$

Then, one has

$$\begin{aligned}|u_i| \le \|\underline{\boldsymbol{D}}_i\|&\left[k_{c1}(1+k_{c2}) + \omega_0^2\|\boldsymbol{J}\| + d_{\max}\right.\\ &\left. + \left\|\boldsymbol{F}^T(t_0 + 3O_T)\right\|d_{\max}\right].\end{aligned} \tag{A23}$$

By the proper selection of controller gains k_{c1} and k_{c2} such that (33), one can ensure that $|u_i|$ remains less than the maximum allowable torque, i.e., $|u_i(t)| < u_{\max}, t \ge t_s$. □

REFERENCES

[1] B. Xiao, Q. Hu, D. Wang, and E. K. Poh, "Attitude tracking control of rigid spacecraft with actuator misalignment and fault," *IEEE Trans. Control Syst. Technol.*, vol. 21, no. 6, pp. 2360–2366, Nov. 2013.

[2] D. Bustan, S. H. Sani, and N. Pariz, "Adaptive fault-tolerant spacecraft attitude control design with transient response control," *IEEE/ASME Trans. Mechatronics*, vol. 19, no. 4, pp. 1404–1411, Aug. 2014.

[3] Y. M. Zhang and J. Jiang, "Bibliographical review on reconfigurable fault-tolerant control systems," *Annu. Rev. Control*, vol. 32, no. 2, pp. 229–252, Dec. 2008.

[4] Y. W. Liang, L. W. Ting, and L. G. Lin, "Study of reliable control via an integral-type sliding mode control scheme," *IEEE Trans. Ind. Electron.*, vol. 59, no. 8, pp. 3062–3068, Aug. 2012.

[5] A. M. Zou and K. D. Kumar, "Adaptive fuzzy fault-tolerant attitude control of spacecraft," *Control Eng. Practice*, vol. 19, no. 1, pp. 10–21, Jan. 2011.

[6] J. Jin, S. Ko, and C. K. Ryoo, "Fault tolerant control for satellites with four reaction wheels," *Control Eng. Practice*, vol. 16, no. 10, pp. 1250–1258, Oct. 2008.

[7] S. Yin, S. Ding, X. Xie, and H. Huo, "A review on basic data-driven approaches for industrial process monitoring," *IEEE Trans. Ind. Electron.*, vol. 61, no. 11, pp. 6418–6428, Nov. 2014.

[8] S. Yin, X. Li, H. Gao, and O. Kaynak, "Data-based techniques focused on modern industry: An overview," *IEEE Trans. Ind. Electron.*, vol. 62, no. 1, pp. 657–667, Jan. 2015.
[9] X. G. Yan and C. Edwards, "Adaptive sliding-mode-observer-based fault reconstruction for nonlinear systems with parametric uncertainties," *IEEE Trans. Ind. Electron.*, vol. 55, no. 11, pp. 4029–4036, Nov. 2008.
[10] R. H. Kwong and D. L. Yonge-Mallo, "Fault diagnosis in discrete-event systems: Incomplete models and learning," *IEEE Trans. Syst., Man, Cybern. B, Cybern.*, vol. 41, no. 1, pp. 118–130, Feb. 2011.
[11] W. R. Williamson, J. L. Speyer, V. T. Dang, and J. Sharp, "Fault detection and isolation for deep space satellites," *J. Guid., Control, Dyn.*, vol. 32, no. 5, pp. 1570–1584, Aug. 18–21, 2009.
[12] R. J. Patton, F. J. Uppal, S. Simani, and B. Polle, "Robust FDI applied to thruster faults of a satellite system," *Control Eng. Practice*, vol. 18, no. 9, pp. 1093–1109, Sep. 2011.
[13] A. Nasir and E. M. Atkins, "Fault tolerance for spacecraft attitude management," in *Proc. AIAA Guid., Navigat., Control Conf.*, Toronto, ON, Canada, 2010, pp. 1–23.
[14] P. Martella, A. Tramutola, and M. Montagna, "Fine gyroless attitude control: The SAX experience," in *Proc. 15th IFAC Symp. Autom. Control Aerosp.*, Bologna Forli, Italy, 2002, pp. 67–76.
[15] J. W. Kruk *et al.*, "FUSE in-orbit attitude control with two reaction wheels and no gyroscopes," in *Conf. Future EUV/UV Visible Space Astrophys. Missions Instrum.*, Bellingham, WA, USA, 2003, pp. 274–285.
[16] B. Xiao, Q. L. Hu, and Y. M. Zhang, "Fault-tolerant attitude control for flexible spacecraft without angular velocity magnitude measurement," *J. Guid., Control, Dyn.*, vol. 34, no. 5, pp. 1556–1561, Sep./Oct. 2011.
[17] A. Tayebi, "Unit quaternion-based output feedback for the attitude tracking problem," *IEEE Trans. Automat. Contr.*, vol. 53, no. 6, pp. 1516–1520, Jul. 2008.
[18] H. H. Choi, "Sliding-mode output feedback control design," *IEEE Trans. Ind. Electron.*, vol. 55, no. 11, pp. 4047–4054, Nov. 2008.
[19] S. Islam and X. P. P. Liu, "Robust sliding mode control for robot manipulators," *IEEE Trans. Ind. Electron.*, vol. 58, no. 6, pp. 2444–2453, Jun. 2011.
[20] K. C. Veluvolu and Y. C. Soh, "Discrete-time sliding-mode state and unknown input estimations for nonlinear systems," *IEEE Trans. Ind. Electron.*, vol. 56, no. 9, pp. 3443–3452, Sep. 2009.
[21] K. C. Veluvolu and Y. C. Soh, "High-gain observers with sliding mode for state and unknown input estimations," *IEEE Trans. Ind. Electron.*, vol. 56, no. 9, pp. 3386–3393, Sep. 2009.
[22] C. P. Tan, X. Yu, and Z. Man, "Terminal sliding mode observers for a class of nonlinear systems," *Automatica*, vol. 46, no. 8, pp. 1401–1404, Aug. 2010.
[23] J. M. Daly and D. W. L. Wang, "Output feedback sliding mode control in the presence of unknown disturbances," *Syst. Control Lett.*, vol. 58, no. 3, pp. 188–193, Mar. 2009.
[24] S. Nicosia and P. Tomei, "Nonlinear observer and output feedback attitude control of spacecraft," *IEEE Trans. Aerosp. Electron Syst.*, vol. 28, no. 4, pp. 970–977, Oct. 1992.
[25] I. Ali, G. Radice, and J. Kim, "Backstepping control design with actuator torque bound for spacecraft attitude maneuver," *J. Guid., Control, Dyn.*, vol. 33, no. 1, pp. 254–259, Jan./Feb. 2010.
[26] A. H. J. d. Ruiter, "Adaptive spacecraft attitude control with actuator saturation," *J. Guid., Control, Dyn.*, vol. 33, no. 5, pp. 1692–1695, Sep./Oct. 2010.
[27] B. Xiao, Q. L. Hu, and Y. M. Zhang, "Adaptive sliding mode fault tolerant attitude tracking control for flexible spacecraft under actuator saturation," *IEEE Trans. Control Syst. Technol.*, vol. 20, no. 6, pp. 1605–1612, Nov. 2012.
[28] B. Xiao, Q. L. Hu, Y. M. Zhang, and X. Huo, "Fault tolerant tracking control of spacecraft with attitude-only measurement under actuator failures," *J. Guid., Control, Dyn.*, vol. 37, no. 3, pp. 838–849, 2014.

Bing Xiao received the B.S. degree in mathematics from Tianjin Polytechnic University, Tianjin, China, in 2007 and the M.S. and Ph.D. degrees in engineering from Harbin Institute of Technology, Harbin, China, in 2010 and 2014, respectively.

He is currently a Professor with the College of Engineering, Bohai University, Jinzhou, China. His current research interests include spacecraft attitude control, fault diagnosis, fault-tolerant control, robot control, and mechatronics.

Mingyi Huo is currently working toward the B.S. degree in the Department of Control Science and Engineering, Harbin Institute of Technology, Harbin, China.

Her main research interests include satellite attitude control system design.

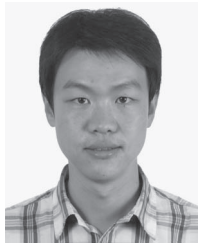

Xuebo Yang received the B.S. degree in automation from Northeast Forestry University, Harbin, China, in 2004, the M.S. degree in control science and engineering from Harbin Engineering University, Harbin, China, in 2007, and the Ph.D. degree in control science and engineering from Harbin Institute of Technology, Harbin, China, in 2011.

He is currently an Associate Professor with the Research Institute of Intelligent Control Systems, Harbin Institute of Technology. His current research interests include spacecraft control and robust and optimal control for aerospace applications.

Youmin Zhang (SM'07) received the B.S., M.S., and Ph.D. degrees with a specialization in automatic control from Northwestern Polytechnical University, Xi'an, China, in 1983, 1986, and 1995, respectively.

He is currently a Professor with the Department of Mechanical and Industrial Engineering, Faculty of Engineering and Computer Science, Concordia University, Montreal, QC, Canada. His current research interests include condition monitoring, health management, fault diagnosis, and fault-tolerant (flight) control systems; the cooperative guidance, navigation, and control of unmanned aerial/space/ground/surface vehicles; dynamic systems modeling, estimation, and identification of advanced control and signal processing techniques for the diagnosis, prognosis, and health management of safety-critical systems, renewable energy systems, and smart grids; and manufacturing processes. He is the author of four books and over 350 journal and conference papers and book chapters.

Dr. Zhang is a Senior Member of the American Institute of Aeronautics and Astronautics (AIAA) and a member of the Technical Committee (TC) for several scientific societies, including the International Federation of Automatic Control TC on Fault Detection, Supervision, and Safety for Technical Processes, the AIAA Infotech@Aerospace Program Committee on Unmanned Systems, the IEEE Robotics and Automation Society TC on Aerial Robotics and Unmanned Aerial Vehicles, the American Society of Mechanical Engineers/IEEE TC on Mechatronics and Embedded Systems and Applications, and the International Conference on Unmanned Aircraft Systems (ICUAS) Association Executive Committee. He has been invited to deliver plenary talks at international conferences/workshops and research seminars worldwide more than 50 times. He is the Editor-in-Chief of the *Journal of Instrumentation, Automation and Systems*, an Editorial Board Member, and/or an Editor-at-Large, a Senior Editor, or an Associate Editor of six other international journals (including three newly launched journals on unmanned systems). He has served as a General Chair, a Program Chair, a Program Vice Chair, and an International Program Committee Member of many international conferences, e.g., he was the General Chair of the 2014 International Conference on Intelligent Unmanned Systems, Montreal, QC, Canada; the Program Chair of the 2014 ICUAS, Orlando, FL, USA; and one of the General Chairs of the 2015 ICUAS, Denver, CO, USA.